

1 **First assessment of Aeolus L2A particle backscatter coefficient** 2 **retrievals in the Eastern Mediterranean**

3

4 Antonis Gkikas¹, Anna Gialitaki^{1,5,6}, Ioannis Binietoglou¹, Eleni Marinou¹, Maria Tsihla¹, Nikolaos
5 Siomos¹, Peristera Paschou^{1,5}, Anna Kampouri^{1,7}, Kalliopi Artemis Voudouri^{1,5}, Emmanouil
6 Proestakis¹, Maria Mylonaki², Christina-Anna Papanikolaou², Konstantinos Michailidis⁵, Holger
7 Baars³, Anne Grete Straume⁴, Dimitris Balis⁵, Alexandros Papayannis², Tomasso Parrinello⁸ and
8 Vassilis Amiridis¹

9

10 ¹Institute for Astronomy, Astrophysics, Space Applications and Remote Sensing, National Observatory of Athens,
11 Athens, Greece

12 ²Laser Remote Sensing Unit, Department of Physics, National and Technical University of Athens, Athens, Greece

13 ³Leibniz-Institut für Troposphärenforschung e.V., Leipzig, Germany

14 ⁴European Space Agency (ESA/ESTEC), Noordwijk, Netherlands

15 ⁵Laboratory of Atmospheric Physics, Aristotle University of Thessaloniki, Thessaloniki, Greece

16 ⁶Department of Physics and Astronomy, University of Leicester, Leicester, United Kingdom

17 ⁷Department of Meteorology and Climatology, School of Geology, Aristotle University of Thessaloniki,
18 54124 Thessaloniki, Greece

19 ⁸European Space Agency (ESA/ESRIN), Frascati, Italy

20 Corresponding author: Antonis Gkikas (agkikas@noa.gr)

21

22 **Abstract**

23 Since 2018, the Aeolus satellite of the European Space Agency (ESA) acquires wind HLOS
24 (horizontal line-of-sight) profiles throughout the troposphere and up to the lower stratosphere, filling
25 a critical gap of the Global Observing System (GOS). Aeolus, carrying ALADIN (Atmospheric LAsER
26 Doppler INstrument), the first UV HSRL (High Spectral Resolution Lidar) Doppler lidar ever placed
27 in space, along with wind HLOS profiles provides also vertically resolved optical properties of
28 particulates (aerosols, clouds). The present study focuses on the assessment of Aeolus L2A particulate
29 backscatter coefficient (baseline 2A11), retrieved by the Standard Correct Algorithm (SCA), in the
30 Eastern Mediterranean, a region hosting a variety of aerosol species. Ground-based retrievals
31 acquired by lidar instruments operating in Athens (capital of Greece), Thessaloniki (north Greece)
32 and Antikythera (southwest Greece) serve as reference. All lidar stations provide routine
33 measurements to the PANACEA (PANhellenic infrastructure for Atmospheric Composition and
34 climatE chAnge) network. A set of ancillary data including sunphotometric observations
35 (AERONET), reanalysis products (CAM5, MERRA-2), satellite observations (MSG-SEVIRI,

36 MODIS-Aqua) and backward trajectories modelling (FLEXPART) are utilized towards an optimum
37 characterization of the probed atmospheric conditions under the absence of a classification scheme in
38 Aeolus profiles. First, emphasis is given on the assessment of Aeolus L2A backscatter coefficient
39 under specific aerosol scenarios over the Antikythera island. Due to the misdetection of the cross-
40 polar component of the backscattered lidar signal, Aeolus underestimates the aerosol backscatter
41 coefficient by up to 33% when non-spherical mineral particles are recorded (10th July 2019). A good
42 performance is revealed on 3rd July 2019, when horizontally homogeneous loads of fine spherical
43 particles are confined below 4 km. For other two cases (8th July 2020, 5th August 2020), due to noise
44 issues, the Aeolus performance downgrades in terms of depicting the stratification of aerosol layers
45 composed of particles of different origin. According to the statistical assessment analysis for 43
46 identified cases, it is revealed a poor-to-moderate performance for the unfiltered (aerosols plus
47 clouds) Aeolus profiles which improves substantially when cloud contaminated profiles are excluded
48 from the collocated sample. This improvement is evident at both Aeolus vertical scales (regular, 24
49 bins and mid-bin, 23 bins) and it is justified by the drastic reduction of the bias (from 0.45 Mm⁻¹sr⁻¹
50 to 0.27 Mm⁻¹sr⁻¹ for SCA and from 0.69 Mm⁻¹sr⁻¹ to 0.37 Mm⁻¹sr⁻¹ for SCA mid-bin) and root-mean-
51 square-error (from 2.00 Mm⁻¹sr⁻¹ to 1.65 Mm⁻¹sr⁻¹ for SCA and from 1.88 Mm⁻¹sr⁻¹ to 1.00 Mm⁻¹sr⁻¹
52 for SCA mid-bin) scores. In vertical, the Aeolus performance downgrades at the lowermost bins due
53 to either the contamination from surface signals or the increased noise levels for the aerosol retrievals.
54 Among the three PANACEA stations, the best agreement is found at the remote site of Antikythera
55 with respect to the urban sites of Athens and Thessaloniki. Finally, all key Cal/Val aspects necessary
56 for future relevant studies, the recommendations for a possible Aeolus follow-on mission and an
57 overview of the ongoing related activities are thoroughly discussed.

58

59 **1. Introduction**

60 Atmospheric aerosols constitute a critical component of the Earth system by acting as a major
61 climatic driver (Charlson et al., 1992; Boucher et al., 2013; Li et al., 2022) whereas upon deposition
62 they can affect terrestrial (Okin et al., 2004) and marine ecosystems (Jickells et al., 2005; Li et al.,
63 2018). It is also well documented that they affect several anthropogenic activities with concomitant
64 economic impacts (Middleton et al., 2018; Kosmopoulos et al., 2018). In addition, aerosols
65 accumulation at large concentrations cause an air quality degradation (Kanakidou et al., 2011) with
66 adverse health effects (Pöschl, 2005; Lelieveld et al., 2015) increasing the mortality rates (Health
67 Effects Institute, 2019; Pye et al., 2021). Therefore, their multifaceted role in multidisciplinary
68 research fields highlights the growing scientific concern in understanding and describing the
69 emission, removal, and transport mechanisms governing airborne particles' life cycle. Due to their

70 pronounced heterogeneity, aerosol burden exhibits a remarkable spatiotemporal variability thus
71 imposing deficiencies in depicting adequately its features and constraints towards a robust assessment
72 of the induced impacts.

73 Passive satellite sensors, providing columnar retrievals of aerosol optical depth (AOD), have
74 been able to reproduce adequately aerosol loads across various spatiotemporal scales. This has been
75 justified via the assessment of AOD versus corresponding sun-photometric measurements (e.g., Wei
76 et al., 2019). Nevertheless, the main drawback arises from the sensors' inability to provide
77 information in vertical. Therefore, this deficiency hampers a reliable quantification of the suspended
78 particles' load within the planetary boundary layer (PBL), related to health impacts. Moreover, it is
79 not feasible to depict the three-dimensional structure of transported loads in the free troposphere,
80 linked to aerosol-cloud-radiation interactions and associated impacts on atmospheric dynamics (Pérez
81 et al., 2006; Gkikas et al., 2018; Haywood et al., 2021). Likewise, passive aerosol observations are
82 not suitable for monitoring stratospheric long-lived plumes that affect aerosol-chemistry interactions
83 and perturb the radiation fields (Solomon et al., 2022). On the contrary, ground-based lidars, relying
84 on active remote sensing techniques, obtain vertical profiles of aerosol optical properties at high
85 vertical and temporal resolution, through multi-wavelength and polarization measurements. Such
86 observations are performed either at networks distributed across Europe (EARLINET; Papalardo et
87 al., 2014; PollyNET; Baars et al., 2016; Engelmann et al., 2016), United States (MPLNET; Campbell
88 et al., 2002), Asia (AD-NET; Sugimoto et al., 2014) and South America (LALINET; Guerrero-
89 Rascado et al., 2016), or at dedicated experimental campaigns (Ansmann et al., 2011; Weinzierl et
90 al., 2016) or even at open seas (Bohlmann et al., 2018). The reproduction of aerosols' vertical
91 structure at global (Liu et al., 2008) and regional (Marinou et al., 2017; Proestakis et al., 2018) scales
92 has been realized through the utilization of measurements acquired by the Cloud-Aerosol Lidar and
93 Infrared Pathfinder Satellite Observation (CALIOP; Winker et al., 2009) and the Cloud-Aerosol
94 Transport System (CATS; McGill et al., 2015; Lee et al., 2019) mounted on the CALIPSO (Cloud-
95 Aerosol Lidar and Infrared Pathfinder Satellite Observation) satellite and the International Space
96 Station (ISS), respectively.

97 On 22nd August 2018, the European Space Agency (ESA) launched its Earth Explorer wind
98 mission, Aeolus, which was a major step forward for Earth Observations (EO) and atmospheric
99 sciences. The Aeolus satellite carries ALADIN (Atmospheric LAsER Doppler INstrument), the first
100 space-based high spectral resolution (HSRL) Doppler wind lidar worldwide. ALADIN emits a linear
101 polarized beam which after going through a quarter-wave plate is transmitted with a circular
102 polarization (at 355 nm) and receives the co-polarized backscatter from molecules and
103 particles/hydrometeors in two separate channels (Ansmann et al., 2007; Flamant et al., 2008). The

104 main mission product is profiles of the horizontally projected line-of-sight winds, and spin-off
105 products are the backscatter and extinction coefficient profiles from particles and hydrometeors. The
106 key scientific objective of Aeolus is to improve numerical weather forecasts and our understanding
107 of atmospheric dynamics and their impacts on climate (Stoffelen et al., 2005; Isaksen and Rennie,
108 2019; Rennie and Isaksen, 2019). After about 1.5 years of instrument and algorithm improvements,
109 the Aeolus L2B wind product was of such good quality (e.g., Witschas et al., 2020; Lux et al., 2020;
110 Martin et al., 2021) that the European Centre for Medium Range Forecasts (ECMWF) could start
111 operational assimilation (January 2020). In May 2020, three further European weather forecast
112 institutes (DWD, Météo-France and the UK MetOffice) started the operational assimilation of Aeolus
113 winds. All meteorological institutes reported that Aeolus winds had significant positive impact on the
114 short and medium term forecasts. The most beneficial impact is found in remote areas (Tropics, S.
115 Hemisphere, polar regions) less covered by other direct wind observations (e.g. ECMWF 2020;
116 Rennie et al., 2021).

117 A series of errors induced by the instrument, by the retrieval algorithm, or by the type of
118 scatterers probed by ALADIN can affect the product quality. It is therefore necessary to perform
119 extensive calibration and validation (Cal/Val) studies utilizing independent reference measurements
120 (e.g. ground-based, aircraft). This task has been performed by the Aeolus Cal/Val community,
121 responding to the Aeolus Announcement of Opportunity to perform product calibration and
122 validation. Such critical tasks are prerequisites to the acceptance of the Mission as “fit for purpose”
123 as it is underlined in the Aeolus Implementation Cal/Val Plan. In contrast to Aeolus wind retrievals,
124 a limited number of studies are focused on the quality of the L2A optical properties. Abril-Gago et
125 al. (2022) performed a statistical validation versus ground-based observations from three Iberian
126 ACTRIS/EARLINET lidar stations affected mainly by dust and continental/anthropogenic aerosols.
127 In their Cal/Val study, they processed AERONET optical properties related to particles’ size and
128 nature along with HYSPLIT air-mass backtrajectories towards characterizing the prevailing aerosol
129 conditions. Baars et al. (2021) reported an excellent agreement between Aeolus and Polly^{XT} particle
130 backscatter profiles and adequate agreement of extinction and lidar ratio profiles, between 4 and 12
131 km, for a case of long-range transport of wildfire smoke particles from California to Leipzig
132 (Germany).

133 Here we focus on the comparison of Aeolus L2A particle backscatter coefficient profiles
134 against ground-based profile observations acquired at three lidar stations (Antikythera, Athens,
135 Thessaloniki) contributing to the Greek National Research Infrastructure (RI) PANACEA, an
136 ACTRIS component (<https://www.actris.eu>). All stations are located in the Eastern Mediterranean, a

137 crossroad of air masses (Lelieveld et al., 2002) carrying particles of different nature. The broader
138 Greek area encompasses a variety of aerosol species consisting of: (i) pollutants from industrialized
139 European regions (Gerasopoulos et al., 2003; 2009), (ii) dust aerosols from the nearby deserts (Balis
140 et al., 2004; Papayannis et al., 2005; Gkikas et al., 2016, Marinou et al., 2017), (iii) anthropogenic
141 aerosols from urban areas and megacities (Kanakidou et al., 2011), (iv) biomass burning particles
142 originating in the eastern Europe and the Black Sea (Amiridis et al., 2009; 2010; 2012), (v) smoke
143 aerosols subjected to transport at planetary scale (Baars et al., 2019; Gialitaki et al., 2020), (vi) sea-
144 salt particles produced by bursting bubbles during whitecap formation attributed to wind-wave
145 interactions (e.g. Varlas et al., 2021), (vii) biogenic particles such as airborne fungi and pollen grains
146 (Richardson et al., 2019) and (viii) volcanic ash mixed with sulfate aerosols ejected at high altitudes
147 from explosive Etna eruptions (Zerefos et al., 2006, Kampouri et al., 2021).

148 The manuscript is structured as follows. In Section 2, a brief overview of the Aeolus satellite
149 and the ALADIN instrument is given. The key elements of the Standard Correct Algorithm (SCA)
150 are summarized in Section 3. The technical information of the ground-based lidars as well as the
151 description of aerosols' regime, in the surrounding area of the PANACEA stations, are presented in
152 Section 4. The collocation criteria between ground-based and spaceborne profiles are described in
153 Section 5. The assessment of Aeolus L2A product under various aerosol scenarios and for the whole
154 collocated sample are discussed in Section 6. The Cal/Val aspects, the recommendations for future
155 relevant studies and the necessary upgrades on ALADIN observational capabilities and Aeolus L2A
156 data content are highlighted in Section 7. Finally, the main findings and the conclusions are drawn in
157 Section 8.

158

159 **2. AEOLUS - ALADIN**

160

161 A brief description of Aeolus' orbital features, ALADIN's observational geometry and its
162 measurement configuration is given in the current section. This short introduction serves as the
163 starting point for the reader to be familiar with Aeolus' nomenclature. Further details and a more
164 comprehensive overview of the Aeolus satellite mission can be found at ESA technical reports (ESA,
165 1999; 2008; 2016) and at recently published studies (e.g., Lux et al., 2020; Witschas et al., 2022; Lux
166 et al., 2022).

167 ESA's Aeolus satellite, named by the 'keeper of winds' according to the Greek mythology
168 (Ingmann and Straume, 2016), flies in a polar sun-synchronous orbit circling the Earth at an altitude

169 of 320 km with a repeat cycle of 7 days (Kanitz et al., 2019a; Straume et al., 2019). The orbital plane
170 forms an angle of 97° with the equatorial plane, the ground track velocity is about 7.2 km/sec and a
171 complete circle around the Earth takes about 90 minutes for each orbit (Lux et al., 2020; Witschas et
172 al., 2020; Straume et al., 2020). Aeolus is flying over the terminator between day and night
173 (dawn/dusk orbits), with its solar panels facing towards the sun direction for minimizing the solar
174 background illumination (Kanitz et al., 2019).

175 ALADIN, the single payload on the Aeolus satellite platform, is an HSRL lidar (Shiple et
176 al., 1983) equipped with a Nd-YAG laser that emits short laser pulses (~ 40 to 70 mJ, Witschas et al.,
177 2020) of a circular polarized light at ~ 355 nm with a 50.5 Hz repetition frequency. The photons that
178 are backscattered from molecules and particulates (aerosols, cloud droplets and ice crystals) at
179 atmospheric altitudes lower than 30 km are collected by a Cassegrain telescope of 1.5 m diameter.
180 The collected photons are directed to the Mie optical channel (Fizeau interferometer) for the analysis
181 of the Doppler shift induced by particulates while the molecular return signals (Rayleigh) are analyzed
182 in two sequentially coupled Fabry–Pérot interferometers (Witschas et al., 2020).

183 ALADIN provides wind and particulate vertically resolved retrievals along the Line-Of-Sight
184 (LOS) by pointing the Earth at a slant angle of 35° off-nadir (see Figure 1 in Flament et al., (2021))
185 which corresponds to an angle of about 37.6° with the Earth surface, due to its curvature. In contrast
186 to CALIOP and CATS, ALADIN can retrieve particulate optical products without requiring an a
187 priori assumption of the lidar ratio (S), which is characterized by a remarkable variability among
188 aerosol types due to its dependency on particles' shape, composition and size distribution (Müller et
189 al., 2007). However, ALADIN only measures the co-polar part of the atmospheric backscatter and at
190 a single wavelength. Therefore, it is very challenging the discrimination between aerosols and clouds
191 and to distinguish further among their subtypes.

192 The instrument detector design allows the sampling of the atmospheric backscatter in 24
193 vertical bins, with a varying resolution from 0.25 (near surface) to 2 km (upper atmosphere). The
194 laser pulses are integrated on-board the satellite along the satellite flight direction, to yield
195 measurements of ~ 3 km resolution (integration of ~ 20 laser pulses). During the on-ground data
196 processing, the measurements are accumulated further to yield an “*observation*” (also called a *Basic*
197 *Repeat Cycle (BRC)*), which corresponds to a distance of ~ 90 km. The L2A optical properties product
198 which will be described in the next section, derived by the so-called Standard Correct Algorithm
199 (SCA) (Flament et al., 2021), are provided at the observation scale (on a horizontal resolution of ~ 90
200 km) and are available through the Aeolus Online Dissemination System (<https://aeolus-ds.eo.esa.int>).

201

202

203 3. Standard Correct Algorithm (SCA)

204 In the current Cal/Val study, we are assessing the performance of the Aeolus L2A particulate
205 products derived by the Standard Correct Algorithm (SCA). Here, we are providing a short overview
206 of the SCA whereas its complete description is available in the Algorithm Theoretical Baseline
207 Document (ATBD; Flamant et al., 2021). The SCA product is derived from the measured signals in
208 the Mie and Rayleigh channels, which are dependent on the instrument calibration constants (K_{ray} ,
209 K_{mie}), the channel cross-talk coefficients C_1 , C_2 , C_3 and C_4 , the laser pulse energy (E_0) and the
210 contributions from the pure molecular (X) and particulate (Y) signals (see Equations 1 and 2 in
211 Flament et al. (2021)). The latter ones, at each bin, result from the vertical integration of the
212 backscatter (either molecular or particulate) where the squared one-way transmission through the
213 atmosphere is taken into account (see Equations 3 and 4 in Flament et al. (2021)).

214 The separation of the molecular and particle signals on each channel is imperfect, due to the
215 HSRL instrument design, which makes necessary a cross-talk correction. The channel cross-talk
216 corresponding to the transmission of the Rayleigh-Brillouin spectrum (depending on the temperature,
217 pressure and the Doppler shift) through the Rayleigh and Mie channels is expressed by the calibration
218 coefficients C_1 and C_4 , respectively (Flament et al., 2021). The other two coefficients, C_2 and C_3 ,
219 refer to the transmission of a Mie spectrum (depending on the Doppler shift) through the Mie and
220 Rayleigh channels, respectively. Along with the cross-talk coefficients, the instrument calibration
221 constants (K_{ray} , K_{mie}) (see in Flament et al., 2021) are included in the AUX_CAL files.

222 Finally, the cross-talk corrected signals, normalized with the range bin thickness and corrected
223 by the range between the satellite and the observed target, are utilized for the retrieval of the vertically
224 resolved backscatter (β) and extinction (α) coefficients. The former, at each bin, is derived by the Y/X
225 ratio multiplied with the molecular backscatter coefficient (see Equations 9 and 10 in Flament et al.,
226 2021) computed from the pressure and temperature ECMWF simulated fields according to Collis and
227 Russel (1976). For the L2A extinction retrievals, derived via an iterative process from top to bottom,
228 the normalized integrated two-way transmission (NITWT) is applied, using measured and simulated
229 pure molecular signals, under the assumption that the particles' extinction at the top-most bin is zero
230 (see equations 11-14 in Flament et al., 2021). This consideration makes the downwards solution of
231 the integral equations quite sensitive to the noise within the topmost bin (at altitudes ~20-25 km),
232 which is used as reference for the normalization, particularly under low SNR conditions due to the
233 low molecular density. This is a challenge frequently faced for the Aeolus observations due to the
234 weaker measured signals than those of the pre-launch expectations (Reitebuch et al., 2020) as well as
235 to the possible presence of stratospheric aerosols within the top-most range bin or above. In principle,
236 the extinction is retrieved recursively taking into account the attenuation from the overlying bins and

237 by contrasting observed and simulated molecular signals. By differentiating two consecutive bins,
238 unrealistically high positive or negative extinctions can be retrieved (see Fig. 10 in Flament et al.,
239 (2021)) resulting from fluctuations between strong and weak attenuation.

240 In the case of negative extinction values, the SCA algorithm regularizes the solution by
241 resetting to zero (Flament et al., 2021), which can lead to an underestimation of the partial column
242 transmission. In order to compensate the impacts of the aforementioned issues, it has been shown by
243 error propagation calculations (see equations 18 and 19 in Flament et al. (2021)), that averaging two
244 consecutive bins the retrieved extinction becomes more reliable at the expense of the vertical
245 resolution (23 bins; “mid-bin” vertical scale). In contrast to SCA, in the SCA mid-bin negative
246 extinction values can be found since the zero-flooring constraint is not implemented. For consistency
247 reasons, the averaging between two neighboring bins is applied also in the backscatter coefficient
248 thus allowing the derivation of the lidar ratio.

249 The inherent weaknesses of the SCA algorithm have been mitigated in the Maximum
250 Likelihood Estimation (MLE) algorithm (Ehlers et al., 2022). Its main principle relies on the
251 exploitation of all available information and the definition of constraints on the positivity of the
252 retrieved optical properties and on the expected range of the lidar ratio. Under these restrictions, the
253 particle extinction is derived when the particle backscatter is available and vice versa. According to
254 the evaluation versus ground-based observations and SCA end-to-end simulated optical products, it
255 is revealed a remarkable improvement (up to one order) on the precision of the extinction and the
256 lidar ratio due to effective noise dampening. Moreover, there is also a beneficial impact on the co-
257 polar backscatter coefficient. Another new algorithm that outperforms SCA is the AEL algorithm
258 (adjusted from the EarthCARE-ATLID algorithms) providing a feature mask (AEL-FM) at the
259 highest available resolution and aerosol/clouds extinction and lidar ratios via a multi-scale optimal
260 estimation method (AEL-PRO). Both MLE and AEL retrievals have been released at a more recent
261 baseline (2A14) than those used in the current study (2A11) and for this reason are omitted from our
262 Cal/Val analysis.

263

264 **4. Ground-based lidars (PANACEA)**

265 The ground-based observational datasets used herein, are taken from stations contributing to
266 the PANhellenic infrastructure for Atmospheric Composition and climatE chAnge (PANACEA)
267 initiative. Within PANACEA, different measurement techniques and sensors are utilized in a
268 synergistic way for monitoring the atmospheric composition and climate change related parameters
269 in Greece.

270 The locations of the stations providing routine measurements to the PANACEA network are
271 shown in Figure 1-i. For the assessment analysis of Aeolus L2A products, we utilize available
272 measurements from PANACEA stations, namely Antikythera (ANT), Athens (ATH) and
273 Thessaloniki (THE), equipped with multiwavelength polarization lidar systems. All stations comply
274 with the quality-assurance criteria established within EARLINET (e.g. see Freudenthaler et al., 2016)
275 so as to assure the provision of high-quality aerosol related products. Consequently, the derived
276 datasets can be considered for any validation purpose. To ensure the homogeneity and the consistency
277 of the optical property profiles derived from the adverse lidar systems operating at each station, the
278 Single Calculus Chain algorithm (SCC; D' Amico et al., 2016; Mattis et al., 2016) was used; an
279 automatic processing chain for lidar data, developed within EARLINET. All systems employ multiple
280 detectors, operating either in the photon-counting or analog mode. Herein elastically and inelastically
281 backscattered signals at 355 and 387 nm, were used to evaluate Aeolus products. The optical property
282 profiles were derived using the Raman and Klett-Fernald-Sassano inversion methods (Ansmann et al.
283 1992; Fernald, 1984; Klett, 1981; Sasano and Nakame, 1984) during night-time and daytime
284 measurements respectively.

285

286 *4.1 Antikythera*

287 Regular lidar measurements have been performed at the PANGAEA observatory (PANhellenic
288 GEophysical observatory of Antikythera; lat=35.86° N, lon=23.31° E, alt=193 m asl.) contributing to
289 this study. The lidar system deployed at PANGAEA is operated by the National Observatory of Athens
290 (NOA). It is a Polly^{XT} (Engelmann et al., 2016) multi-wavelength Polarization-Raman-Water vapor
291 lidar, designed for unattended, continuous operation. Polly^{XT} deploys an Nd:YAG laser which emits
292 linearly polarized light at 355, 532 and 1064 nm. The radiation elastically and inelastically
293 backscattered from aerosol, cloud particles, nitrogen (at 387 and 607 nm) and water vapor (at 407
294 nm) molecules, is collected using a near-range (spherical mirror of 50 mm diameter, focal length
295 f=250 mm and 2.2 mrad field of view (FOV)) and a far-range receiver (Newtonian telescope with a
296 300 mm diameter primary mirror, f=900 m and 1 mrad FOV) at a raw vertical resolution of 7.5m.
297 The combined use of the near-range and far-range receivers allows for the retrieval of the aerosol
298 optical properties from 500 m up to ~12-14 km above the ground. A detailed description of the
299 technical characteristics of Polly^{XT} can be found in Engelmann et al. (2016).

300

301 *4.2 Athens*

302 The Laser Remote Sensing Unit of the National and Technical University of Athens, Greece
303 (LRSU; NTUA; lat=37.96° N, lon=23.78° E, alt=200 m asl.), is part of the EARLINET since May

304 2000. Currently, the Athens lidar station performs simultaneous measurements with two different
305 lidar systems, EOLE and DEPOLE. The EOLE lidar is an advanced 6-wavelength elastic
306 backscatter/Raman lidar system able to provide the aerosol backscatter coefficient at 355, 532 and
307 1064 nm, the aerosol extinction coefficient at 355 and 532 nm and water vapor mixing ratio profiles
308 in the troposphere. EOLE is based on a pulsed Nd:YAG laser system and a 300 mm diameter
309 receiving Cassegrain telescope ($f=600$ mm, $FOV = 1.5$ mrad) which collects all elastically
310 backscattered lidar signals (355-532-1064 nm), as well as generated by the vibrational Raman effect
311 (by atmospheric N_2 at 387-607 nm and by H_2O at 407 nm). The full overlap (i.e. the altitude from
312 which upwards the whole lidar beam is within the telescope FOV) of EOLE is reached at,
313 approximately, 812 m a.s.l.. EOLE has been validated within EARLINET at hardware level by two
314 intercomparison campaigns (Matthias et al., 2004), in order to fulfill the standardized criteria.

315 The DEPOLE lidar is a depolarization lidar, able to provide profiles of the aerosol backscatter
316 coefficient and the linear particle/volume depolarization ratio at 355 nm. DEPOLE is based on a
317 pulsed Nd:YAG laser system which emits linearly polarized light at 355 nm. The elastically
318 backscattered lidar signals at 355 nm are collected by a 200 m diameter Dall-Kirkham/Cassegrain
319 telescope ($f=600$ mm, $FOV=3.13$ mrad) and the full overlap is reached at, approximately, 500 m a.s.l..
320

321 *4.3 Thessaloniki*

322 Thessaloniki's multiwavelength Polarization Raman lidar system (THELISYS) belongs to the
323 Laboratory of Atmospheric Physics that is located at the Physics Department of the Aristotle
324 University of Thessaloniki (lat = 40.63° N, lon = 22.96° E, a.s.l. = 50m). Thessaloniki is a member
325 station of the EARLINET since 2000, providing almost continuous measurements, according to the
326 network schedule (every Monday morning, ideally close to 12:00 UTC, and every Monday and
327 Thursday evening) and during extreme events (e.g., Saharan dust outbreaks, smoke transport from
328 biomass burning, volcanic eruptions) and satellite overpasses. THELISYS has been validated within
329 EARLINET at hardware level by two intercomparison campaigns (Matthias et al., 2004), in order to
330 fulfill the standardized criteria. The system is based on the first (1064 nm), second (532 nm), and
331 third harmonic (355 nm) frequency of a compact, pulsed Nd:YAG laser emitted with a 10 Hz
332 repetition rate. THELISYS setup includes three elastic backscatter channels at 355, 532 and 1064nm,
333 two nitrogen Raman channels at 387 nm and 607nm, and two polarization sensitive channels at 532
334 nm. The acquisition system is based on a LICEL Transient Digitizer working in both the analogue
335 and photon counting (250 MHz) mode. The vertical resolution of the elastic raw signal at 355 nm is
336 equal to 3.75 m and is recorded in both analog and photon counting mode. The full overlap height is

337 almost 800m a.s.l. A detailed description of THELISYS can be found in Siomos et al. (2018) and
338 Voudouri et al. (2020).

339

340 *4.4. Aerosols' load variability in the vicinity of the PANACEA sites*

341 The variability of the atmospheric aerosol load in the vicinity of three PANACEA stations
342 (Fig. 1-i) is discussed in this section. The aim of this introductory analysis is to investigate the
343 horizontal homogeneity of the aerosol optical depth (AOD) in the respective broader areas, playing a
344 key role in the comparison of ground-based and spaceborne profiles, which are not spatially
345 coincident as it will be shown in Section 5. For the purposes of this analysis, we have processed the
346 mid-visible (550 nm) columnar AOD retrievals, over the period 2008-2017, acquired by the MODIS
347 sensor, mounted on the Aqua polar orbiting satellite. More specifically, we have analyzed the Level
348 2 (L2; swaths; 5-min segments) MODIS-Aqua AODs, obtained by the latest version (Collection 6.1)
349 of the operational retrieval algorithms (Remer et al., 2008; Levy et al., 2013; Sayer et al., 2013). The
350 aforementioned data are accessible via the Level 1 and Atmosphere Archive and Distribution System
351 (LAADS) Distributed Active Archive Center (DAAC) (<https://ladsweb.modaps.eosdis.nasa.gov/>, last
352 access: 17 June 2022).

353 For each station, we have calculated the arithmetic mean of AODs, representative over the
354 period 2008-2017, within progressively larger circular areas, with radii spanning from 10 to 100 km
355 with an incremental step of 10 km (Fig. 1-ii). Figure 1-iii illustrates the resulting AODs for each
356 station (x labels) and at each radius (colored bars). In order to ensure the reliability of the obtained
357 results, only the best (QA=3) MODIS-Aqua AOD L2 retrievals are considered whereas the spatial
358 averages (computed individually for each circle) are calculated only when the satellite observations
359 are simultaneously available at all circles. In the urban areas of Athens (ATH) and Thessaloniki
360 (THE), the contribution of anthropogenic aerosols on the columnar load fades for increasing radii.
361 On the contrary, at Antikythera (ANT), the spatial AOD means remain almost constant revealing a
362 horizontal homogeneity of the aerosol load in the broader area. An alternative way to compare the
363 differences in the AOD spatial representativeness between the urban (ATH, THE) and the remote
364 (ANT) sites has been performed. Fig. 1-iv illustrates the normalized values for each radius with
365 respect to the AOD levels of the inner circle (i.e., up to 10 km distance from the station). In both
366 urban sites the values are lower than one (dashed line), decreasing steadily in THE and smoothly in
367 ATH after an abrupt reduction from 10 to 20 km. In ANT, the blue curve resides almost on top of the
368 dashed line throughout the circles radii (i.e., range of distances) indicating the absence of significant
369 horizontal variation of the aerosol load suspended in the surrounding area of the station.

370 A key aspect which has not been adequately addressed in Fig. 1-iii, is the temporal variability
371 of aerosol loads since the spatiotemporally averaged AODs “hide” such information. A useful
372 measure for this purpose is the coefficient of variation (CV), defined as the ratio of the standard
373 deviation and the arithmetic mean of AOD (Anderson et al., 2003; Shinozuka and Redemann, 2011).
374 Figure 1-v displays the CV values (expressed in percentage), computed for the period 2008-2017, for
375 each circle at each station. The highest levels (up to 90%) are recorded in Antikythera whereas lower
376 values (up to 70%) are recorded in THE and the lowest ones are found in ATH (up to 60%). This
377 discrepancy is mainly attributed to the higher frequency of dust outbreaks affecting the southern parts
378 of Greece in contrast to the central and northern sectors of the country (Gkikas et al., 2013; 2016). It
379 is noted that all the PANACEA sites are also under the impact of advected loads composed by
380 anthropogenic/biomass particles originating at distant areas. Nevertheless, their frequency of
381 occurrence and their concentration is rarer and weaker, respectively, than those of the advected
382 Saharan dust. Between the remote (ANT) and urban (ATH, THE) sites there is clear difference of the
383 CV dependence with respect to the circle radius. In ANT, the CVs increase steadily from the inner to
384 the outer circle while an opposite tendency is found in THE and ATH. The increasing trend in ANT
385 is mainly regulated by the range of the Saharan plumes transported towards southwest Greece. On
386 the contrary, the declining trend revealed in the two main Greek cities indicates that the temporal
387 variability of the local sources (i.e., two first cycles) is more pronounced. For completeness, we have
388 also computed the spatial autocorrelation (Anderson et al., 2003; Shinozuka and Redemann, 2011)
389 among the averaged AODs of each circle area. The correlation matrices for each station are presented
390 in Fig. S1. Among the three PANACEA sites, the R values in Athens (Fig. S1-i) drop rapidly, with
391 respect to the first circle (10 km radius), highlighting the strong spatial contrast of AODs between the
392 city and the surrounding areas. For the outer domains, this transition becomes significantly smoother
393 and the R values are higher than 0.90 in most of the combinations indicating a spatial coherence. In
394 Thessaloniki (Fig. S1-iii), the pattern of the R values onto the correlation matrix is similar with those
395 of Athens but the high R values (> 0.89) indicate a better spatial AOD homogeneity according to
396 Anderson et al. (2003). Finally, under the absence of local sources in Antikythera and strong
397 horizontal AOD variability in the vicinity, the computed R value between the inner (10 km radius)
398 and the outer (100 km radius) circle is higher than 0.94 and increases at shorter distances.

399 **5. Collocation between Aeolus and ground-based lidars**

401 The assessment of Aeolus L2A backscatter profiles has been performed against the
402 corresponding measurements acquired at the three EARLINET/PANACEA lidar stations. In Figure
403 2, three examples of the collocation between ground-based and spaceborne retrievals are illustrated
404 in order to describe our approach as well as to clarify points needed in the discussion of the evaluation

405 results (Section 6). At each station, we identify the observations (BRCs), considering their
406 coordinates at the beginning of the ALADIN scan, falling within a circle of 120 km radius (black
407 dashed circle) centered at the station coordinates (black dot). Based on the defined spatial criterion,
408 applied for each case, the number of BRCs residing within the 120 km circle should be at least one
409 and cannot be more than three. We denote each one of them, along the ALADIN measurement track
410 (white stripe), with different colors (red, blue and magenta) in Fig. 2. The green arrow shows the
411 flight direction of the satellite for the dusk (ascending) or dawn (descending) orbits. For the ground-
412 based observations, the aerosol backscatter profiles are derived considering a time window of ± 1
413 hour around the satellite overpass. Nevertheless, this temporal collocation criterion has been relaxed
414 or shifted in few cases to improve the quality of the ground-based retrievals (i.e., by increasing the
415 signal-to-noise ratio) as well as to increase the matched pairs with Aeolus L2A profiles. Both
416 compromises are applied since the weather conditions favoring the development of persistent clouds
417 may eliminate the number of simultaneous cases. It is noted, however, when the temporal window is
418 shifted or relaxed we are taking into account the homogeneity of the atmospheric scene (probed by
419 the ground lidar). For the Antikythera station we did not deviate from the pre-defined temporal
420 criterion apart from one case study. In Thessaloniki and Athens, the time departure between Aeolus
421 and ground-based profiles can vary from 1.5 to 2.5 hours. Overall, 43 cases are analyzed out of which
422 15 have been identified over Antikythera, 12 in Athens and the remaining 16 in Thessaloniki.

423 The ground-based profiles are derived under cloud free conditions in contrast to Aeolus L2A
424 backscatter profiles providing aerosol and/or cloud backscatter. Therefore, a cloud screening of the
425 Aeolus data using auxiliary cloud information was applied. In the framework of the present study, the
426 exclusion of cloud contaminated Aeolus profiles relies on the joint processing of the cloud mask
427 product (CLM; <https://www.eumetsat.int/media/38993>; [CLOUD MASK PRODUCT](https://www.eumetsat.int/media/38993)
428 [GENERATION](https://www.eumetsat.int/media/38993)) derived from radiances acquired by the SEVIRI (Spinning Enhanced Visible and
429 Infrared Imager) instrument mounted on the Meteosat Second Generation (MSG4) geostationary
430 satellite (Schmetz et al., 2002). It should be noted, however, that the CLM product serves as an
431 indication of clouds presence, without providing information about their macrophysical properties
432 (i.e., cloud coverage), their phase (i.e., ice, water, mixed) or their categories (i.e., low, middle, high).
433 According to the product user guide (https://www-cdn.eumetsat.int/files/2020-04/pdf_clm_pg.pdf;
434 Section 3.4), artificial straight lines can be found because the ECMWF temperature/humidity fields
435 are not interpolated in time and space. Moreover, due to the limited number of levels of ECMWF
436 temperature profiles, required for the atmospheric correction, the cloud detection in the lower
437 troposphere is impacted. Finally, broken clouds with limited spatial extension as well as thin cirrus
438 are likely misdetected by MSG. In the illustration examples of Figure 2, the grey shaded areas

439 represent the CLM spatial coverage at each PANACEA site. Based on the filtering procedures, the
440 Aeolus L2A backscatter retrievals, throughout the probed atmosphere by ALADIN, are removed from
441 the analysis when the grey shaded areas overlap with a BRC.

442

443 **6. Results**

444 *6.1 Assessment of Aeolus L2A backscatter under different aerosol scenarios*

445 In the first part of the analysis we assess the quality of the Aeolus L2A backscatter under
446 various aerosol regimes aiming to: (i) investigate the capabilities of the ALADIN spaceborne lidar to
447 detect aerosol layers, (ii) investigate how the horizontal homogeneity and vertical structure of the
448 aerosol layers can affect the level of agreement between spaceborne and ground-based retrievals and
449 (iii) demonstrate the synergistic use of various datasets for a better characterization of the prevailing
450 aerosol conditions. All of these aspects are necessary towards a comprehensive Cal/Val study to
451 facilitate the interpretation of our findings and to identify possible upgrades on Aeolus retrievals.
452 Overall, four cases over the Antikythera island (southwest Greece) are analyzed for the Aeolus L2A
453 aerosol backscatter retrievals (Baseline 2A11). The obtained results are depicted in Figure 3. The
454 identified cases have been selected because they are representing some of the most typical aerosol
455 conditions in the E. Mediterranean. Note that for each case we are selecting the nearest Aeolus BRC
456 to station coordinates that falls entire within the circle area.

457 As it has been already mentioned, Aeolus retrievals are provided at coarse spatial (BRC level;
458 ~90 km) and vertical (minimum 250 m) resolution, while currently there is no scene classification
459 scheme. In order to overcome this inherent limitation, as much as possible, several ancillary data and
460 products are utilized in parallel with those of the MSG-SEVIRI CLM product. Based on the
461 FLEXPART v10.4 Lagrangian transport model (Stohl et al., 2005; Ignacio Pisso et al., 2019) we have
462 reproduced the 5-day air masses backtrajectories prior to their arrival at 7 altitudes above the ground
463 station. FLEXPART was driven with 3-hourly meteorological data from the National Centers for
464 Environmental Prediction (NCEP) Global Forecast System (GFS) analyses provided at $0.5^\circ \times 0.5^\circ$
465 resolution and for 41 model sigma pressure levels
466 (https://nomads.ncep.noaa.gov/txt_descriptions/GFS_half_degree_doc.shtml). To depict the spatial
467 patterns of the mid-visible (550 nm) total and speciated AOD, we are relying on the MERRA-2
468 (Modern-Era Retrospective analysis for Research and Applications version 2; Buchard et al., 2017;
469 Randles et al., 2017; Gelaro et al., 2017) and CAMS (Copernicus Atmosphere Monitoring Service;
470 Inness et al., 2019) reanalysis datasets, both providing AODs of high quality (Gueymard and Yang,
471 2020; Errera et al., 2021). Finally, AERONET sun-direct measurements (Level 2.0, Version 3; Giles
472 et al., 2019; Sinyuk et al., 2020) of spectral AODs and Ångström exponent as well as the Fine Mode

473 Fraction (FMF at 500nm) derived from the spectral deconvolution algorithm (O'Neill et al., 2003)
474 are also used for the characterization of the aerosol load and size over the station.

475

476 *6.1.1 Dust advection on 10th of July 2019*

477 The first case refers to the advection of dust aerosols from northwest Africa towards
478 Antikythera with dust-laden air masses crossing southern Italy prior to their arrival from northwest
479 directions (Figure S2). This route of air masses, driven by the prevailing atmospheric circulation
480 (Gkikas et al., 2015), is typical during summer when Saharan aerosols are advected towards the
481 eastern Mediterranean (Balis et al., 2006). MERRA-2 (Fig. S3-i) and CAMS (Fig. S3-ii) show a
482 reduction of AODs (at 550nm) from west to east whereas the large contribution (>80%) of dust
483 aerosols to the total aerosol load is evident in both reanalysis products (results not shown here). The
484 moderate-to-high AOD values are confirmed by the ground-based sunphotometric measurements
485 (Fig. S4) which are associated with low Ångström exponent (calculated between 440 nm and 870
486 nm) values (0.2 – 0.4) and FMF (Fig. S5) lower than 0.35 thus indicating the prevalence of coarse
487 mineral particles (Dubovik et al., 2002). This is further supported from Polly^{XT} measurements (Fig.
488 S6) revealing persistent dust layers associated with volume linear depolarization ratio (VLDR) values
489 of 5-10% at 355 nm, stretched from altitudes close to the ground and up to almost 6 km.

490 This case is suitable for evaluating L2A backscatter retrievals since non-spherical mineral
491 particles are probed by ALADIN, which does not detect the cross-polar component of the
492 backscattered lidar signal. Therefore, a degradation of ALADIN's performance is expected (i.e.,
493 underestimation of the backscatter coefficient and overestimation of the lidar ratio) when aspherical
494 particles (e.g., dust, volcanic ash, cirrus ice crystals) are probed. In Figure 3, the backscatter
495 coefficient step-like vertical profiles from Aeolus at the regular (brown) and mid-bin (black) vertical
496 scales are compared against those acquired by the Polly^{XT} (pink) at 355 nm. The colored dashed lines
497 (Aeolus) and the pink shaded area (Polly^{XT}) correspond to the statistical uncertainty margins of the
498 spaceborne (see Section 2.3.1 in Flament et al., (2021)) and the ground-based (D'Amico et al., 2016)
499 retrievals, respectively. Both refer to the photocounting noise following a Poisson distribution. At a
500 first glance, it is revealed that the geometrical structure of the dust layer, extending from 1 to 6 km,
501 is generally well captured by ALADIN (except at altitude ranges from 1 to 2.5 km), but the
502 backscatter magnitude is constantly underestimated. A fairer comparison requires the conversion of
503 the backscatter retrievals assuming that Polly^{XT} emits circularly polarized radiation (instead of
504 linearly polarized) thus resembling ALADIN. Under the assumption of randomly oriented particles
505 and negligible multiple scattering effects, this transformation is made based on theoretical formulas
506 (Mishchenko and Hovenier, 1995; Roy and Roy, 2008), as it has been shown in Paschou et al. (2021).

507 Following this approach, the Aeolus-like backscatter (i.e., circular co-polar component; blue curve in
508 Fig. 3) is reproduced for the ground-based profiles at altitudes where UV depolarization
509 measurements are available. Thanks to this conversion, the Aeolus-Polly^{XT} negative biases diminish
510 and the Aeolus-like curve resides closer to those of SCA (brown) and SCA mid-bin (black)
511 backscatter levels. The difference between pink and blue backscatter profiles, ranging from 13 to 33%
512 in this specific case, reflects the underdetermination of the particle backscatter coefficient in case of
513 depolarizing aerosols being probed, due to the missing cross-polar backscatter component.

514

515 *6.1.2 Long-range transport of fine aerosols on 3rd July 2019*

516 Under the prevalence of the Etesian winds (Tyrlis and Lelieveld, 2013), anthropogenic
517 aerosols from megacities (Kanakidou et al., 2011) and biomass burning particles originating in the
518 eastern Europe (van der Werf et al., 2017) are transported southwards. Based on the FLEXPART
519 simulations (Fig. S7), the air masses carrying fine particles, gradually descend till their arrival over
520 Antikythera from north-northeastern directions. During early morning hours, when ALADIN probes
521 the atmosphere at a distance of ~90 km westwards of the ground station (dawn orbit; descending),
522 moderate AODs (up to 0.15 at 340 nm), very high Ångström exponent values (>1.2) and FMFs
523 varying from 0.6 to 0.7 are measured with the Cimel sunphotometer (Fig. S8 and Fig. S9). The aerosol
524 load is confined below 2.5 km consisting of spherical particles as it is revealed from the Polly^{XT}
525 volume linear depolarization ratio (VLDR) values, which do not exceed 5% at 355 nm (Fig. S10). In
526 the vicinity of the PANGEA observatory, MERRA-2 (Fig. S11-i) and CAMS (Fig. S11-ii) AODs,
527 mainly attributed to organic carbon, sulphate and sea-salt aerosols, do not exceed 0.2 and they are
528 coherent in spatial terms (i.e., horizontal homogeneity). In this case, Polly^{XT} particle backscatter
529 coefficient profiles coincide with the corresponding Aeolus-like profiles (pink and blue curves are
530 almost overlaid in Fig. 3-ii) since depolarization values are negligible. Under these conditions,
531 ALADIN is capable of reproducing satisfactorily the layer's structure whereas slightly overestimates
532 its intensity with respect to the ground-truth retrievals.

533

534 *6.1.3 Long range transport of fine aerosols on 8th July 2020*

535 On 8th July 2020, the broader area of the Antikythera island was under the impact of moderate-
536 to-high aerosol loads, mainly consisting of organic and sulphate particles, in the western and southern
537 sector of the station, based on CAMS simulated AODs (up to 0.5) (Fig. S12-ii). AERONET
538 measurements yield UV AODs up to 0.5 and Ångström exponent higher than 1.5 during early
539 afternoon (Fig. S13) whereas the FMF is higher than 0.75 throughout the day (Fig. S14). MERRA-2
540 AOD patterns (Fig. S12-i) and speciation (strong contribution from marine and sulphate aerosols to

541 the total aerosol load) are different from those of CAMS, without being very consistent with respect
542 to the ground-based sunphotometer observations (Fig. S13, Fig. S14). Air masses originating in
543 northern Balkans and the Black Sea, after crossing metropolitan areas (i.e., Istanbul, Athens), are
544 advected over ANT at altitudes up to 4 km above surface. A second cluster aloft (>5 km) indicates
545 the convergence of air masses from northwest (Fig. S15). In vertical terms, aerosol layers with local
546 backscatter maxima gradually reducing from 3.5 to 1.5 $\text{Mm}^{-1} \text{sr}^{-1}$ are observed up to 4 km based on
547 Polly^{XT} backscatter coefficient profiles (pink curve, Fig. 3-iii) whereas almost identical values are
548 recorded for the Aeolus-like retrievals (blue curve, Fig. 3-iii) under low VLDR levels (Fig. S16). For
549 this specific case, Aeolus' performance reveals an altitude dependency according to the comparison
550 versus Polly^{XT}. From top to bottom, the weak layer extending from 6 to 8 km, observed in the ground-
551 based lidar profiles is partially evident in the Aeolus retrievals. Aeolus erroneously indicates the
552 presence of an aerosol layer between 3 and 4.5 km due to the overlying noise (i.e., negative
553 backscatter coefficients). This deficiency interprets also the underestimation of the backscatter
554 coefficient at altitudes spanning from 2 to 3 km. Below 2 km, the agreement between ALADIN and
555 Polly^{XT} becomes better, particularly for SCA mid-bin, even though the narrow peak recorded at ~1.2
556 km by Polly^{XT} cannot be reproduced by ALADIN. This might be attributed either to the adjusted RBS
557 at the lowermost bin (1 km thickness) or to the lower accuracy of Aeolus retrievals near the ground
558 due to the attenuation from the overlying layers (Flament et al., 2021).

559

560 *6.1.4 Stratification of spherical and non-spherical particles on 5th August 2020*

561 In the last case, that took place on 5th August 2020, we are investigating the ability of Aeolus
562 to reproduce adequately the vertical structure of an aerosol layer detected up to 4 km based on Polly^{XT}
563 (Fig. 3-iv; pink curve). The “peculiarity” of this study case, as it is revealed by the Polly^{XT} time-
564 height plots of VLDR (Fig. S17), is that spherical fine particles dominate below 2.5 km whereas the
565 presence of non-spherical coarse aerosols above this layer is evident. This stratification results from
566 the convergence of air masses either originating in central Europe or suspending most of their travel
567 above northwest Africa (Fig. S18). According to MERRA-2 (Fig. S19-i) and CAMS (Fig. S19-ii)
568 reanalysis datasets, AODs fade from west to east while both numerical products indicate the
569 coexistence of carbonaceous, sulphate and mineral particles over the area where ALADIN samples
570 the atmosphere (~100 km westwards of Antikythera). During the Aeolus overpass (~04:40 UTC),
571 sunphotometer columnar observations are not available (Fig. S20, Fig. S21). However, one hour later,
572 UV AODs up to 0.4 are recorded and remain relatively constant during sunlight hours. At the same
573 time, intermediate Ångström (0.7 – 1) and FMF (~0.5) values, exhibiting weak temporal variation,
574 indicate a mixing state of fine and coarse aerosols.

575 Aeolus backscatter retrievals at the regular (i.e., SCA; brown curve; Fig. 3-iv) and the mid-
576 bin (i.e., SCA mid-bin; black curve; Fig. 3-iv) vertical scales suffer from noise and retrieval gaps. As
577 a result, Aeolus detects incorrectly an aerosol layer between 5.5 and 8 km under the assumption that
578 clear-sky conditions are appropriately represented in the MSG-SEVIRI imagery and remain constant
579 within the time interval (~6 minutes) of MSG and Aeolus observations. At lower altitudes (2.5 – 4
580 km), due to the suspension of depolarizing mineral particles, a departure is marked between the pink
581 (linear-derived) and blue (Aeolus-like) Polly^{XT} profiles. Both SCA and SCA mid-bin fail to reproduce
582 the backscatter levels of this aerosol layer captured from the ground. In the lowest troposphere (<
583 2km), Aeolus overestimates significantly the backscatter coefficient but reproduces satisfactorily the
584 aerosol layer structure at the mid-bin vertical scale (i.e., SCA mid-bin; black curve; Fig. 3-iv), in
585 contrast to the regular scale (i.e., SCA; brown curve; Fig. 3-iv).

586 A general remark that should be made, is that for the cases analyzed, between the ground-
587 based and spaceborne profiles there is an inconsistency in the vertical representativeness within the
588 lowermost Aeolus bin. Under the absence of the near-field receivers (not considered in our study)
589 Polly^{XT} profiles are reported above ~800 m where the overlap between the laser beam and the receiver
590 telescope field of view is expected to be full. However, the base altitude of the near-surface Aeolus
591 bin is at ~200 m. This can interpret, at some degree, the large positive ALADIN-Polly^{XT} departures
592 at altitudes below 1 km, which are possibly further strengthened by an inappropriate RBS (i.e., low
593 SNR) in the Aeolus retrievals.

594

595 *6.2 Overall assessment and dependencies*

596 In the second part of the analysis, an overall assessment of the Aeolus L2A retrievals is
597 performed by processing all the identified cases (43 in total; see Section 5). Due to the very limited
598 availability of ground-based extinction profiles, only the Aeolus L2A backscatter observations are
599 evaluated. It must be clarified that the evaluation of the Aeolus satellite (SAT) backscatter coefficient
600 is conducted without any conversion (i.e., from total linear to circular co-polar) of the ground-based
601 lidar (GRD) profiles. This has been decided since many of the SAT-GRD collocated samples are
602 derived from the Thessaloniki station. Due to technical issues (related to the polarization purity of the
603 emitted laser beam and the performance of the telescope lenses) no calibrated depolarizing
604 measurements, necessary to derive the Aeolus-like products (Paschou et al., 2021), are available for
605 the study period. Nevertheless, we are not expecting that this consideration, acknowledging that it is
606 imperfect, will affect substantially the robustness of our findings since in most of the study cases the
607 contribution of depolarizing particles is quite low based on the ancillary datasets/products. It is also
608 clarified that the Aeolus QA flags are not taken into account in the current study, since their validity

609 is not yet reliable (Reitebuch et al., 2020) as it has been demonstrated in Abril-Gago et al. (2022).
610 The discussion in the current section is divided in two parts. First, the vertically resolved evaluation
611 metrics are presented separately for the two Aeolus vertical scales, both for the unfiltered and the
612 filtered (cloud-free) profiles (Section 6.2.1). The same analysis format (i.e., SCA vs SCA mid-bin,
613 unfiltered vs filtered) is kept in the second sub-section (Section 6.2.2) where the evaluation results
614 are presented as a function of various dependencies.

615

616 *6.2.1 Vertically resolved evaluation metrics*

617 In Figure 4, the vertically resolved bias (SAT-GRD; upper panel) and root mean square error
618 (RMSE; bottom panel) metrics are depicted for the unfiltered (cloud and aerosol backscatter) Aeolus
619 L2A backscatter retrievals, reported at the regular (left column) and the mid-bin (right column)
620 vertical scales. Bias and RMSE metrics (Wilks, 2019) are used in a complementary way in order to
621 avoid any misleading interpretation of the former score attributed to counterbalancing negative and
622 positive SAT-GRD deviations. For the calculation of the evaluation scores, the GRD profiles have
623 been rescaled to match Aeolus vertical product resolution. To realize, we are calculating the averaged
624 values of the ground-based retrievals residing within the altitude margins of each Aeolus BRC. Note
625 that in the SAT-GRD pairs, all BRCs from all cases are included (right y-axis in Figure 4), satisfying
626 the defined collocation criteria (see Section 5), and they are treated individually. It is reminded that
627 Aeolus L2A data are provided vertically at a constant number of range bins (i.e., 24 for SCA and 23
628 for SCA mid-bin) but their base altitude and their thickness vary along the orbit and from orbit-to-
629 orbit and they are defined dynamically (depending on the optimum SNR). Therefore, since the GRD
630 and SAT profiles are not interpolated in a common predefined grid, we are using as reference the
631 reverse index (with respect to those considered in the SCA retrieval algorithm in which 1 corresponds
632 to the top-most bin) of Aeolus SCA (from 1 to 24; left y-axis in Figs 4 i-a and ii-a) and SCA mid-bin
633 (from 1 to 23; left y-axis in Figs 4 i-b and ii-b) vertical scales.

634 According to our results for the unfiltered Aeolus backscatter profiles (Fig. 4), positive biases
635 (up to $3.5 \text{ Mm}^{-1} \text{ sr}^{-1}$; red bars) are evident, at both vertical scales, at the first three bins (below 2 km).
636 For altitude ranges spanning from 2 to 8 km (bins 4 – 12), mainly positive SAT-GRD biases (up to
637 $\sim 1.5 \text{ Mm}^{-1} \text{ sr}^{-1}$) are recorded for SCA mid-bin whereas for SCA reach up to $\sim 1 \text{ Mm}^{-1} \text{ sr}^{-1}$ in absolute
638 terms. Similar tendencies are evident at the highest altitudes ($> 8 \text{ km}$) but the magnitude of the SAT-
639 GRD offsets becomes lower ($< 0.5 \text{ Mm}^{-1} \text{ sr}^{-1}$). Between the two Aeolus vertical scales, SCA mid-bin
640 performs better than SCA up to $\sim 8 \text{ km}$ (bin 12) and similar aloft, as it is shown by the RMSE profiles
641 (bottom panel in Fig. 4). Nevertheless, the most important finding is that Aeolus is not capable to
642 reproduce satisfactorily the backscatter profiles as it is revealed by the RMSE levels, which are

643 maximized near the ground ($\sim 8 \text{ Mm}^{-1} \text{ sr}^{-1}$), are considerably high (up to $6 \text{ Mm}^{-1} \text{ sr}^{-1}$) in the free
644 troposphere and are minimized ($< 1 \text{ Mm}^{-1} \text{ sr}^{-1}$) at the uppermost bins. Our findings are highly
645 consistent with those presented in Abril-Gago et al. (2022), who performed a validation of Aeolus
646 L2A particle backscatter coefficient against reference measurements obtained at three
647 ACTRIS/EARLINET sites in the Iberian Peninsula. Several factors contribute to the obtained height-
648 dependent SAT-GRD discrepancies. Near the ground, the observed maximum overestimations are
649 mainly attributed to the: (i) contamination of the ALADIN lidar signal by surface reflectance, (ii)
650 increased noise in the lowermost bins (caused by the non-linear approach retrieving the backscatter
651 coefficient) as it has been pointed out also in the atmospheric simulations cases I and II in Ehlers et
652 al. (2022) and (iii) limited vertical representativeness of the GRD profiles below 1 km. On the
653 contrary, in the free troposphere, the cloud contamination on spaceborne retrievals plays a dominant
654 role on the occurrence of ALADIN backscatter overestimations with respect to the cloud-free ground-
655 based retrievals. From a statistical point of view, it must also be mentioned that the robustness of the
656 bias and RMSE metrics decreases for the increasing altitudes due to the reduction of the number of
657 the SAT-GRD matchups (right y-axis in Fig. 4) participating in the calculations.

658 The assessment analysis has been repeated after removing Aeolus profiles when clouds are
659 detected by MSG-SEVIRI (grey shaded areas in Fig. 1) within a BRC (colored rectangles in Fig. 1).
660 By contrasting Figures 4 and 5 (evaluation metrics for the filtered profiles), an expected improvement
661 of the level of agreement between SAT and GRD is visible. This translates into a drastic reduction of
662 bias and RMSE levels at altitude ranges up to 5-6 km (\sim bin 10). Between bins 2 and 5 slight
663 underestimations (blue bars) and overestimations (red bars) are found for SCA (Fig. 5 i-a). On the
664 contrary, for the SCA mid-bin (Fig. 5 i-b) low positive SAT-GRD offsets are recorded due to the
665 omitted negative backscatter values, as it will be shown in the next section. Above bin 5, SAT-GRD
666 deviations are low in absolute terms, oscillating around zero, for SCA, whereas only positive SAT-
667 GRD biases are recorded for SCA mid-bin, which are maximized ($\sim 0.7 \text{ Mm}^{-1} \text{ sr}^{-1}$) at the highest bins
668 and are associated with limited SAT-GRD matchups (right x-axis in Fig. 5 i-b). The obtained
669 improvements on bias scores become more confident since they are associated with similar strong
670 reductive tendencies on RMSE levels. More specifically, the RMSE spikes of extremely high values
671 recorded in the unfiltered profiles either disappear or weaken in the case of the Aeolus filtered SCA
672 (Fig. 5 ii-a) and SCA mid-bin (Fig. 5 ii-b) backscatter profiles. However, even though the RMSE
673 values at the lowermost bins (close to the ground) are decreased when cloud contaminated Aeolus
674 profiles are eliminated, still the corresponding levels for the filtered profiles are considerably high
675 attributed to the lower SNR and the possible impact of surface returns.

676

677 6.2.2 Scatterplots

678

679

680

681

682

683

684

685

686

687

688

689

690

691

692

693

694

695

696

697

698

699

700

701

702

703

704

705

706

707

708

709

710

711

An alternative approach to assess the performance of Aeolus L2A backscatter is attempted here by reproducing two dimensional histograms for the entire SAT-GRD collocated sample as well as scatterplots resolved based on various dependencies, aiming to investigate the factors determining the level of agreement between spaceborne and ground-based retrievals. More specifically, the dependencies under investigation are those of the: (i) station locations, (ii) BRCs and (iii) orbits (dawn vs dusk). The evaluation metrics have been calculated for all possible combinations of vertical scales (SCA vs SCA mid-bin) and Aeolus profiles (unfiltered vs filtered).

Figure 6 depicts the two-dimensional histograms between GRD (x-axis) and SAT (y-axis) backscatter coefficient for the raw (upper panel) and filtered (bottom panel) Aeolus profiles reported at the SCA (left column) and SCA mid-bin (right column) vertical scales. Note that we have removed SAT-GRD pairs in which Aeolus backscatter exceeds $20 \text{ Mm}^{-1} \text{ sr}^{-1}$ in order to avoid the “contamination” of extreme outliers in the calculated metrics, possibly attributed to the presence of clouds (Proestakis et al., 2019).

Between the SCA and SCA mid-bin unfiltered retrievals, it is found that the correlation coefficients (0.36 and 0.39, respectively) and RMSEs (2.00 and 1.88, respectively) are similar whereas there is an evident difference on the biases ($0.45 \text{ Mm}^{-1} \text{ sr}^{-1}$ and $0.69 \text{ Mm}^{-1} \text{ sr}^{-1}$, respectively). Nevertheless, it is noted that less SAT-GRD pairs are recorded for SCA mid-bin due to the inherent flagging of negative values. After removing cloud-contaminated Aeolus profiles, the amount of the SAT-GRD matchups is reduced by about 55% and 59% for SCA (from 537 to 239) and SCA mid-bin (from 356 to 147), respectively. Nevertheless, thanks to this filtering procedure, the initially observed overestimations for SCA and SCA mid-bin are reduced by ~25% and ~43%, respectively, whereas the RMSE values drop down to 1.65 (SCA) and 1.00 (SCA mid-bin). The better agreement between SAT and GRD, for the filtered Aeolus profiles, is further justified by the increase of the R values (from 0.39 to 0.48) for the SCA mid-bin whereas for SCA there is no positive or negative tendency ($R=0.36$). The spread of the points in the two dimensional space reveals many similarities with the corresponding scatterplots presented in Abril-Gago et al. (2022) for the Iberian ACTRIS/EARLINET stations.

A common feature in all scatterplots, shown in Figure 6, is that most of the positive outliers are found at the lowermost bins (see Figs. 4 and 5). SAT beta can reach up to $20 \text{ Mm}^{-1} \text{ sr}^{-1}$ in contrast to the corresponding GRD levels, which are mainly lower than $2 \text{ Mm}^{-1} \text{ sr}^{-1}$. For SCA (Figs. 6 i-a, 6 ii-a), the majority of the negative SAT-GRD pairs are recorded at the highest bins in which, however, both spaceborne and ground-based backscatter coefficients are noisy. Another cluster of SAT-GRD pairs is those where slight negative Aeolus backscatter values are grouped together with low positive

712 backscatter values retrieved from ground. At the mid-bin vertical scale, for the unfiltered Aeolus
713 profiles (Fig. 6 i-b), the negative SAT backscatter values are masked out resulting in better evaluation
714 metrics (except the increase of bias due to the removal of the negative Aeolus backscatter) with
715 respect to the regular vertical scale. Among the four scatterplots, the best agreement between Aeolus
716 and ground-based retrievals is revealed for the SCA mid-bin filtered profiles (Fig. 6 ii-b) attributed
717 to the coincident elimination of the negative and the extreme positive Aeolus backscatter coefficient.

718 Figure 7 depicts the overall scatterplot between ground-based and spaceborne retrievals as a
719 function of the three PANACEA sites (colored categories). The associated evaluation scores are
720 summarized in Table 1 and 2 for the unfiltered and filtered Aeolus profiles, respectively. The majority
721 of the extreme positive outliers of unfiltered SCA retrievals (Fig. 7 i-a) are recorded in Thessaloniki
722 and Athens. According to our results, significant biases ($0.73 \text{ Mm}^{-1} \text{ sr}^{-1}$ for ATH and $0.83 \text{ Mm}^{-1} \text{ sr}^{-1}$
723 for THE) and high RMSE values ($2.26 \text{ Mm}^{-1} \text{ sr}^{-1}$ for ATH and $2.60 \text{ Mm}^{-1} \text{ sr}^{-1}$ for THE) are found. At
724 Antikythera island (ANT), the biases are quite low and equal to $0.06 \text{ Mm}^{-1} \text{ sr}^{-1}$ and 13.6% in absolute
725 and relative terms, respectively (Table 1). In all stations, for the unfiltered SCA mid-bin retrievals,
726 the absolute SAT-GRD departures become larger whereas the RMSE decreases in ANT/THE and
727 increases in ATH. Regarding the temporal covariation between SAT and GRD retrievals, a noticeable
728 improvement is evident in ANT (i.e., R increases from 0.49 to 0.57). For the quality-assured Aeolus
729 profiles (Table 2), all evaluation metrics converge towards the ideal scores for SCA mid-bin whereas
730 mainly positive tendencies (i.e., better agreement) are evident for SCA. Overall, among the three
731 stations the best performance of Aeolus is recorded at the Antikythera island.

732 Between dawn (descending) and dusk (ascending) orbits, better bias and RMSE scores are
733 computed when Aeolus is flying during early morning hours while better R values are found during
734 early afternoon satellite overpasses. However, our orbit-wise results are not robust since the number
735 of Aeolus overpasses is not evenly distributed (about 85% of the SAT-GRD matchups are acquired
736 during dawn orbits). Among the three BRCs (red, blue or magenta), which can satisfy the defined
737 SAT-GRD spatial criterion (see Section 5) the best metrics are found for the red BRC residing most
738 of the cases closer to the station site.

739

740 **7. Discussion on Cal/Val aspects and recommendations**

741

742 Throughout this assessment analysis, several critical points have been identified and
743 highlighted that should be addressed adequately towards a comprehensive Cal/Val study of the
744 Aeolus L2A products. These aspects can: (i) serve as guidelines for future relevant studies, (ii)
745 improve our understanding about the advantages/limitations of Aeolus data in terms of their

746 usefulness and applicability in aerosol-related studies and (iii) suggest possible upgrades regarding
747 ALADIN's observational capabilities, the considerations of the applied retrieval algorithms and the
748 content of information in Aeolus L2A data.

749 A fair comparison of Aeolus L2A backscatter versus linear-derived retrievals acquired from
750 ground-based lidars, when depolarizing particles are recorded, requires the conversion of the latter
751 ones to circular co-polar (Aeolus-like) following Paschou et al. (2021). Nevertheless, it should be
752 acknowledged that the theoretical assumptions can be invalid either due to the orientation of the
753 suspended particles (e.g., mineral dust; Ulanowski et al., 2007; Daskalopoulou et al., 2021; Mallios
754 et al., 2021) or due to multiple scattering effects within optically thick aerosol layers (Wandinger et
755 al., 2010). The lack of aerosols/clouds discrimination in Aeolus L2A data forces the synergistic
756 implementation of ancillary data in order to remove cloud contaminated Aeolus profiles from the
757 collocated sample with the cloud-free ground-based profiles. Nevertheless, it should be noted that the
758 cloud removal itself is not perfect. In our case, we are relying on MSG-SEVIRI cloud observations,
759 which are available at high temporal frequency (every 15 min) thus allowing a very good temporal
760 collocation with Aeolus. The indirect cloud-mask filtering applied to our analysis, leads to a
761 substantial improvement of the level of agreement between spaceborne and ground-based retrievals.
762 Despite its success, our proposed approach provides a sufficient and acceptable solution, but
763 undoubtedly cannot be superior to the utility of a descriptive classification scheme on Aeolus retrieval
764 algorithms similarly done in CALIOP-CALIPSO (Liu et al., 2019; Zeng et al., 2019).

765 Aeolus retrievals are available at coarse along-track resolution (~90 km). This imposes
766 limitations on their evaluation against point measurements, which are further exacerbated at sites
767 where the heterogeneity of aerosol loads in the surrounding area of the station is pronounced, taking
768 into account that the spatial collocation between spaceborne and ground-based retrievals is not exact.
769 Numerical outputs from reanalysis datasets (e.g., MERRA-2, CAMS) can be utilized as an indicator
770 of aerosols' burden horizontal variation, taking advantage of their complete spatial coverage, their
771 availability at high temporal frequency and their reliability in terms of total AOD (Innes et al., 2019;
772 Gueymard and Yang, 2020). Nevertheless, such data are better to be utilized in a qualitative rather
773 than a quantitative way, particularly in terms of aerosol species, since they cannot be superior of
774 actual aerosol observations. Over areas with a complex terrain, vertical inconsistencies between
775 ground-based and satellite profiles (reported above ground where its height is defined with respect to
776 the WGS 84 ellipsoid), not physically explained, can be recorded. For the derivation of the evaluation
777 scores, it is required a rescaling of the ground-based profiles, acquired at finer vertical resolution, in
778 order to match the dynamically defined Aeolus' range bin settings. Nevertheless, due to this
779 transformation, the shape of the raw ground-based profile can be distorted and the magnitude of the

780 retrieved optical properties can be modified substantially thus affecting the evaluation metrics. This
781 artifact is evident in cases where the vertical structure of the aerosol layers is highly variable thus
782 hindering Aeolus capability to reproduce accurately their geometrical features. Finally, the
783 consideration of backward trajectories can assist the characterization of the probed atmospheric scene
784 by Aeolus. Potentially, they can be also used as an additional criterion for the optimum selection of
785 Aeolus BRC for the collocation with the ground-based measurements. However, possible limitations
786 may arise due to temporal deviations among FLEXPART run, the Aeolus overpass and ground-based
787 retrievals, which might be critical taking into account the strong spatiotemporal variability of aerosol
788 loads across various scales.

789

790 **8. Conclusions**

791 The limited availability of vertically resolved aerosol products from space constitutes a major
792 deficiency of the Global Observing System (GOS). The launch of the Aeolus ESA satellite was a
793 major step towards this direction whereas the forthcoming EarthCARE satellite mission (Illingworth
794 et al., 2015) will accelerate further these efforts. ALADIN, the single payload of the Aeolus satellite,
795 constitutes the first UV HSRL Doppler lidar ever placed in space and it is optimized to acquire HLOS
796 wind profiles towards advancing numerical weather prediction (Rennie et al., 2021). ALADIN also
797 retrieves independently the extinction and backscatter coefficients of aerosols and clouds (grouped as
798 particulates according to Aeolus' nomenclature) via the implementation of the SCA algorithm.

799 The current work focuses on the assessment of the SCA backscatter coefficients versus
800 ground-based retrievals acquired routinely by lidar systems operating in Athens, Thessaloniki, and
801 Antikythera. The aforementioned stations contribute to the PANACEA Greek National Research
802 Infrastructure (Greek ACTRIS component) and to the European Aerosol Research Lidar Network
803 (EARLINET; Pappalardo et al., 2014). Overall, 43 cases are analyzed out of which 12 have been
804 identified in the urban site of Athens, 16 in Thessaloniki and 15 in the remote site of the Antikythera
805 island.

806 In the first part of the analysis, focus was given on the assessment of Aeolus L2A particle
807 backscatter coefficient, under specific aerosol scenarios, versus the corresponding measurements
808 obtained at the Antikythera island (southwest Greece). As expected, the misdetection of the cross
809 polarized lidar return signals, induces an underestimation (ranging from 13% to 33%) of Aeolus L2A
810 backscatter when depolarizing mineral particles are probed (case of 10th July 2019). For the case of
811 3rd July 2019, when aerosol loads of moderate intensity, consisting mainly of spherical particles, are
812 confined below 4 km and they are homogeneous in the surrounding area of the station, Aeolus' SCA
813 backscatter product is capable in reproducing quite well the ground-based profile in terms of shape

814 and magnitude. For the cases of 8th July 2020 and 5th August 2020, Aeolus performance in terms of
815 depicting complex stratified aerosol layers (composed of particles of different origin), as these are
816 observed from ground, downgrades due to noise in the cross-talk corrected molecular and particulate
817 signals.

818 From our statistical assessment analysis, it has been revealed that the removal of cloud
819 contaminated spaceborne profiles, achieved via the synergy with MSG-SEVIRI cloud observations,
820 results in a significant improvement of the product performance. Unfortunately, the poor evaluation
821 metrics at the lowermost bins (attributed to either the surface reflectance or the increased noise levels
822 for the Aeolus retrievals and to the overlap issues for the ground-based profiles) are still evident after
823 the cloud filtering procedure. Between the two Aeolus vertical scales, the computed evaluation
824 metrics do not provide strong evidence of which of them performs better. Among the three stations
825 (ATH, ANT, THE) considered here, the best agreement was found in the remote site of Antikythera
826 island in contrast to the urban sites of Athens and Thessaloniki. All key Cal/Val aspects, serving as
827 guidelines and potential recommendations for future studies, have been discussed thoroughly.

828 In the current work, we emphasized only on the particle backscatter coefficient due to the
829 limited number of ground-based extinction profiles. A wider assessment analysis is ongoing in the
830 framework of the Aeolus L2A Cal/Val study performed within EARLINET. Finally, the best
831 assessment of Aeolus L2A products is expected versus the purpose-built eVe lidar (Paschou et al.,
832 2021). Thanks to its configuration, eVe can mimic Aeolus' observational geometry and test the
833 validity of the theoretical formulas applied for the derivation of the Aeolus-like backscatter from the
834 linearly polarized emission ground-based systems. The first correlative Aeolus-eVe measurements
835 have been performed in the framework of the Joint Aeolus Tropical Atlantic Campaign (JATAC),
836 that took place in Cape Verde in September 2021. Correlative measurements are also acquired during
837 the ESA-ASKOS experimental campaign (Mindelo, Cabo Verde). The geographical location of Cabo
838 Verde, situated on the "corridor" of the Saharan transatlantic transport (Gkikas et al., 2022), is ideal
839 for assessing Aeolus performance when non-spherical mineral particles from the nearby deserts are
840 advected westwards.

841

842 **Acknowledgments**

843 Antonis Gkikas was supported by the Hellenic Foundation for Research and Innovation (H.F.R.I.)
844 under the "2nd Call for H.F.R.I. Research Projects to support Post-Doctoral Researchers" (project
845 acronym: ATLANTAS, project number: 544). Vassilis Amiridis acknowledges support from the
846 European Research Council (grant no. 725698; D-TECT). NOA members acknowledge support from
847 the Stavros Niarchos Foundation (SNF). We acknowledge support of this work by the project

848 “PANhellenic infrastructure for Atmospheric Composition and climatE change” (MIS 5021516)
849 which is implemented under the Action “[Reinforcement of the Research and Innovation](#)
850 [Infrastructure](#)”, funded by the Operational Programme "Competitiveness, Entrepreneurship and
851 Innovation" (NSRF 2014-2020) and co-financed by Greece and the European Union (European
852 Regional Development Fund). We thank the ACTRIS-2 and ACTRIS preparatory phase projects that
853 have received funding from the European Union’s Horizon 2020 Framework Program for Research
854 and Innovation (grant agreement no. 654109) and from European Union’s Horizon 2020 Coordination
855 and Support Action (grant agreement no. 739530), respectively. This research was also supported by
856 data and services obtained from the PANhellenic Geophysical Observatory of Antikythera
857 (PANGEA) of the National Observatory of Athens (NOA). We acknowledge support by ESA, in the
858 framework of the Aeolus+Innovation (Aeolus+I) call, under Contract No. 4000133130/20/I-BG//.

859

860 **Data availability**

861 Aeolus Baseline 11 L2A data were obtained from the ESA Aeolus Online Dissemination System
862 available at <https://aeolus-ds.eo.esa.int/oads/access/>.

863

864 **References**

865 Abril-Gago, J., Guerrero-Rascado, J. L., Costa, M. J., Bravo-Aranda, J. A., Sicard, M., Bermejo-
866 Pantaleón, D., Bortoli, D., Granados-Muñoz, M. J., Rodríguez-Gómez, A., Muñoz-Porcar, C.,
867 Comerón, A., Ortiz-Amezcu, P., Salgueiro, V., Jiménez-Martín, M. M., and Alados-Arboledas, L.:
868 Statistical validation of Aeolus L2A particle backscatter coefficient retrievals over
869 ACTRIS/EARLINET stations on the Iberian Peninsula, *Atmos. Chem. Phys.*, 22, 1425–1451,
870 <https://doi.org/10.5194/acp-22-1425-2022>, 2022.

871

872 Amiridis, V., Balis, D. S., Giannakaki, E., Stohl, A., Kazadzis, S., Koukouli, M. E., and Zanis, P.:
873 Optical characteristics of biomass burning aerosols over Southeastern Europe determined from UV-
874 Raman lidar measurements, *Atmos. Chem. Phys.*, 9, 2431–2440, [https://doi.org/10.5194/acp-9-2431-](https://doi.org/10.5194/acp-9-2431-2009)
875 2009, 2009.

876

877 Amiridis, V., Giannakaki, E., Balis, D. S., Gerasopoulos, E., Pytharoulis, I., Zanis, P., Kazadzis, S.,
878 Melas, D., and Zerefos, C.: Smoke injection heights from agricultural burning in Eastern Europe as
879 seen by CALIPSO, *Atmos. Chem. Phys.*, 10, 11567–11576, [https://doi.org/10.5194/acp-10-11567-](https://doi.org/10.5194/acp-10-11567-2010)
880 2010, 2010.

881

882 Amiridis, V., Zerefos, C., Kazadzis, S., Gerasopoulos, E., Eleftheratos, K., Vrekoussis, M., Stohl, A.,
883 Mamouri, R.E., Kokkalis, P., Papayannis, A., et al.: Impact of the 2009 Attica wildfires on the air
884 quality in urban Athens, *Atmos. Environ.*, 46, 536–544,
885 <https://doi.org/10.1016/j.atmosenv.2011.07.056>, 2012.

886

887 Amodeo, Aldo, D'Amico, Giuseppe, Giunta, Aldo, Papagiannopoulos, Nikolaos, Papayannis, Alex,
888 Argyrouli, Athina, Mylonaki, Maria, Tsaknakis, Georgios, Kokkalis, Panos, Soupiona, Ourania,
889 Tzanis, Chris. (2018). ATHLI16: the ATHens Lidar Intercomparison campaign. EPJ Web of
890 Conferences. 176. 09008. 10.1051/epjconf/201817609008.

891

892 Anderson, T. L., Charlson, R. J., Winker, D. M., Ogren, J. A., and Holmén, K.: Mesoscale Variations
893 of Tropospheric Aerosols, *J. Atmos. Sci.*, 60, 119–136, [https://doi.org/10.1175/1520-](https://doi.org/10.1175/1520-0469(2003)060<0119:MVOTA>2.0.CO;2)
894 [0469\(2003\)060<0119:MVOTA>2.0.CO;2](https://doi.org/10.1175/1520-0469(2003)060<0119:MVOTA>2.0.CO;2), 2003.

895

896 Ansmann, A., Petzold, A., Kandler, K., Tegen, I., Wendisch, M., Müller, D., Weinzierl, B., Müller,
897 T. and Heintzenberg, J.: Saharan Mineral Dust Experiments SAMUM–1 and SAMUM–2: what have
898 we learned?, *Tellus B: Chemical and Physical Meteorology*, 63(4), 403–429, doi:10.1111/j.1600-
899 0889.2011.00555.x, 2011.

900

901 Ansmann, A., Wandinger, U., Riebesell, M., Weitkamp, C., Michaelis, W.: Independent measurement
902 of extinction and backscatter profiles in cirrus clouds by using a combined raman elastic-backscatter
903 lidar, *Applied Optics*, 31, 7113-7131, doi: 10.1364/AO.31.007113, 1992.

904

905 Baars, H., et al. : An overview of the first decade of PollyNET: an emerging network of automated
906 Raman-polarization lidars for continuous aerosol profiling, *Atmos. Chem. Phys.*, 16, 5111–5137,
907 <https://doi.org/10.5194/acp-16-5111-2016>, 2016.

908

909 Baars, H., Ansmann, A., Ohneiser, K., Haarig, M., Engelmann, R., Althausen, D., Hanssen, I., Gausa,
910 M., Pietruczuk, A., Szkop, A., Stachlewska, I. S., Wang, D., Reichardt, J., Skupin, A., Mattis, I.,
911 Trickl, T., Vogelmann, H., Navas-Guzmán, F., Haefele, A., Acheson, K., Ruth, A. A., Tatarov, B.,
912 Müller, D., Hu, Q., Podvin, T., Goloub, P., Veselovskii, I., Pietras, C., Haeffelin, M., Fréville, P.,
913 Sicard, M., Comerón, A., Fernández García, A. J., Molero Menéndez, F., Córdoba-Jabonero, C.,
914 Guerrero-Rascado, J. L., Alados-Arboledas, L., Bortoli, D., Costa, M. J., Dionisi, D., Liberti, G. L.,

915 Wang, X., Sannino, A., Papagiannopoulos, N., Boselli, A., Mona, L., D'Amico, G., Romano, S.,
916 Perrone, M. R., Belegante, L., Nicolae, D., Grigorov, I., Gialitaki, A., Amiridis, V., Soupiona, O.,
917 Papayannis, A., Mamouri, R.-E., Nisantzi, A., Heese, B., Hofer, J., Schechner, Y. Y., Wandinger, U.,
918 and Pappalardo, G.: The unprecedented 2017–2018 stratospheric smoke event: decay phase and
919 aerosol properties observed with the EARLINET, *Atmos. Chem. Phys.*, 19, 15183–15198,
920 <https://doi.org/10.5194/acp-19-15183-2019>, 2019.

921

922 Baars, H., Herzog, A., Heese, B., Ohneiser, K., Hanbuch, K., Hofer, J., Yin, Z., Engelmann, R., and
923 Wandinger, U.: Validation of Aeolus wind products above the Atlantic Ocean, *Atmos. Meas. Tech.*,
924 13, 6007–6024, <https://doi.org/10.5194/amt-13-6007-2020>, 2020.

925

926 Baars, H., Radenz, M., Floutsi, A. A., Engelmann, R., Althausen, D., Heese, B., Ansmann, A.,
927 Flament, T., Dabas, A., Trapon, D., Reitebuch, O., Bley, S., and Wandinger, U.: Californian wildfire
928 smoke over Europe: A first example of the aerosol observing capabilities of Aeolus compared to
929 ground-based lidar, *Geophys. Res. Lett.*, 48, e2020GL092194,
930 <https://doi.org/10.1029/2020GL092194>, 2021.

931

932 Balis, D., Amiridis, V., Nickovic, S., Papayannis, A., and Zerefos, C.: Optical properties of Saharan
933 dust layers as detected by a Raman lidar at Thessaloniki, Greece, *Geophys. Res. Lett.*, 31, L13104,
934 <https://doi.org/10.1029/2004GL019881>, 2004

935

936 Balis, D., Amiridis, V., Kazadzis, S., Papayannis, A., Tsaknakis, G., Tzortzakis, S., Kalivitis, N.,
937 Vrekoussis, M., Kanakidou, M., Mihalopoulos, N., Chourdakis, G., Nickovic, S., Pérez, C.,
938 Baldasano, J., and Drakakis, M.: Optical characteristics of desert dust over the East Mediterranean
939 during summer: a case study, *Ann. Geophys.*, 24, 807–821, [https://doi.org/10.5194/angeo-24-807-](https://doi.org/10.5194/angeo-24-807-2006)
940 2006, 2006.

941

942 Brioude, J., Arnold, D., Stohl, A., Cassiani, M., Morton, D., Seibert, P., Angevine, W., Evan, S.,
943 Dingwell, A., Fast, J.D., Easter, R.C., Pissò, I., Burkhardt, J., Wotawa, G., 2013. The Lagrangian
944 particle dispersion model FLEXPART-WRF version 3.1. *Geosci. Model. Dev.* 6, 1889e1904.
945 <http://dx.doi.org/10.5194/gmd-6-1889-2013>.

946

947 Bohlmann, S., Baars, H., Radenz, M., Engelmann, R., and Macke, A.: Ship-borne aerosol profiling
948 with lidar over the Atlantic Ocean: from pure marine conditions to complex dust–smoke mixtures,
949 *Atmos. Chem. Phys.*, 18, 9661–9679, <https://doi.org/10.5194/acp-18-9661-2018>, 2018.

950

951 Boucher, O., Randall, D., Artaxo, P., Bretherton, C., Feingold, G., Forster, P., Kerminen, V.-M.,
952 Kondo, Y., Liao, H., Lohmann, U., Rasch, P., Satheesh, S., Sherwood, S., Stevens, B., and Zhang,
953 X.: Clouds and Aerosols, in: *Climate Change 2013: The Physical Science Basis. Contribution of*
954 *Working Group I to the Fifth Assessment Report of the Intergovernmental Panel on Climate Change*,
955 edited by Stocker, T., Qin, D., Plattner, G.-K., Tignor, M., Allen, S., Boschung, J., Nauels, A., Xia,
956 Y., Bex, V., and Midgley, P., chap. 7, pp. 571–658, Cambridge University Press, Cambridge, United
957 Kingdom and New York, NY, USA, <https://doi.org/10.1017/CBO9781107415324.016>, 2013.

958

959 Buchard, V., Randles, C. A., da Silva, A. M., Darmenov, A., Colarco, P. R., Govindaraju, R., Ferrare,
960 R., Hair, J., Beyersdorf, A. J., Ziemba, L. D. and Yu, H.: The MERRA-2 aerosol reanalysis, 1980
961 onward. Part II: Evaluation and case studies, *J. Climate*, 30, 6851–6872,
962 <https://doi.org/10.1175/JCLI-D-16-0613.1>, 2017.

963

964 Campbell, J. R., Hlavka, D. L., Welton, E. J., Flynn, C. J., Turner, D. D., Spinhirne, J. D., Scott, V.
965 S., and Hwang, I. H.: Full-time eye-safe cloud and aerosol lidar observation at Atmospheric Radiation
966 Measurement program sites: Instruments and data processing, *J. Atmos. Oceanic Technol.*, 19, 431–
967 442, 2002.

968

969 Charlson, R. J., Schwartz, S. E., Hales, J. M., Cess, R. D., Coakley, J. A., Hansen, J. E., and Hofmann,
970 D. J.: Climate Forcing by Anthropogenic Aerosols, *Science*, 255, 423–430,
971 <https://doi.org/10.1126/science.255.5043.423>, 1992.

972

973 Collis, R. and Russell, P.: Lidar measurement of particles and gases by elastic backscattering and
974 differential absorption, chap. Lidar measurement of particles and gases by elastic backscattering and
975 differential absorption, Springer, Berlin, Heidelberg, 71– 151, [https://doi.org/10.1007/3-540-07743-](https://doi.org/10.1007/3-540-07743-X_18)
976 [X_18](https://doi.org/10.1007/3-540-07743-X_18), 1976.

977

978 Dabas, A.: Generation of AUX_CAL: Detailed Processing Model and Input/Output Data Definition,
979 software, ESA, available at: [https://earth.esa.int/eogateway/documents/20142/1564626/Aeolus-](https://earth.esa.int/eogateway/documents/20142/1564626/Aeolus-Calibration-Processor-Documentation.zip)
980 [Calibration-Processor-Documentation.zip](https://earth.esa.int/eogateway/documents/20142/1564626/Aeolus-Calibration-Processor-Documentation.zip) (last access: 20 February 2022), 2017.

981

982 D'Amico, G., Amodeo, A., Mattis, I., Freudenthaler, V., and Pappalardo, G.: EARLINET Single
983 Calculus Chain – technical – Part 1: Pre-processing of raw lidar data, *Atmos. Meas. Tech.*, 9, 491–
984 507, <https://doi.org/10.5194/amt-9-491-2016>, 2016.

985

986 Daskalopoulou, V., Raptis, I. P., Tsekeri, A., Amiridis, V., Kazadzis, S., Ulanowski, Z., Metallinos,
987 S., Tassis, K., and Martin, W.: Monitoring dust particle orientation with measurements of sunlight
988 dichroic extinction, 15th International Conference on Meteorology, Climatology and Atmospheric
989 Physics (COMECAP 2021), Ioannina, Greece, 26–29 September 2021, Zenodo [conference paper],
990 <https://doi.org/10.5281/zenodo.5075998>, 2021.

991

992 Derrien, M. and Le Gleau, H.: MSG/SEVIRI cloud mask and type from SAFNWC, *Int. J.*
993 *Remote Sens.*, 26, 4707–4732, 2005.

994

995 Dubovik, O., Holben, B. N., Eck, T. F., Smirnov, A., Kaufman, Y. J., King, M. D., Tanré, D., and
996 Slutsker, I.: Variability of Absorption and Optical Properties of Key Aerosol Types Observed in
997 Worldwide Locations, *J. Atmos. Sci.*, 59, 590–608, 2002.

998

999 ECMWF: ECMWF starts assimilating Aeolus wind data, [https://www.ecmwf.int/en/about/media-](https://www.ecmwf.int/en/about/media-centre/news/2020/ecmwf-starts-assimilating-aeolus-wind-data)
1000 [centre/news/2020/ecmwf-starts-assimilating-aeolus-wind-data](https://www.ecmwf.int/en/about/media-centre/news/2020/ecmwf-starts-assimilating-aeolus-wind-data), last access: 12 June 2020, 2020.

1001

1002 Ehlers, F., Flament, T., Dabas, A., Traпон, D., Lacour, A., Baars, H., and Straume-Lindner, A. G.:
1003 Optimization of Aeolus' aerosol optical properties by maximum-likelihood estimation, *Atmos. Meas.*
1004 *Tech.*, 15, 185–203, <https://doi.org/10.5194/amt-15-185-2022>, 2022.

1005

1006 Engelmann, R., Kanitz, T., Baars, H., Heese, B., Althausen, D., Skupin, A., Wandinger, U.,
1007 Komppula, M., Stachlewska, I. S., Amiridis, V., Marinou, E., Mattis, I., Linné, H., and Ansmann, A.:
1008 The automated multiwavelength Raman polarization and water-vapor lidar Polly^{XT}: the neXT
1009 generation, *Atmos. Meas. Tech.*, 9, 1767–1784, <https://doi.org/10.5194/amt-9-1767-2016>, 2016.

1010

1011 Errera, Q., Y. Bennouna, M. Schulz, H.J. Eskes, S. Basart, A. Benedictow, A.-M. Blechschmidt, S.
1012 Chabrillat, H. Clark, E. Cuevas, H. Flentje, K.M. Hansen, U. Im, J. Kapsomenakis, B. Langerock, K.
1013 Petersen, A. Richter, N. Sudarchikova, V. Thouret, A. Wagner, Y. Wang, T. Warneke, C. Zerefos,
1014 Validation report of the CAMS global Reanalysis of aerosols and reactive gases, years 2003-2020,

1015 Copernicus Atmosphere Monitoring Service (CAMS) report, CAMS84_2018SC3_D5.1.1-2020.pdf,
1016 June 2021, doi:10.24380/8gf9-k005.

1017 European Space Agency (ESA): The four candidate Earth explorer core missions: Atmospheric
1018 dynamics mission, ESA Report for Mission Selection ESA SP, 1233, 145 pp., 1999
1019

1020 European Space Agency (ESA): ADM-Aeolus Science Report, ESA SP-1311, 121 pp., available at:
1021 <https://earth.esa.int/documents/10174/1590943/AEOL002.pdf> (last access: 14 June 2022), 2008.
1022

1023 European Space Agency (ESA): “ADM-Aeolus Mission Requirements Document”, ESA EOP-
1024 SM/2047, 57 pp., available at: [http://esamultimedia.esa.int/docs/EarthObservation/ADM-
1025 Aeolus_MRD.pdf](http://esamultimedia.esa.int/docs/EarthObservation/ADM-Aeolus_MRD.pdf) (last access: 2 November 2019), 2016.
1026

1027 Fernald, F. G.: Analysis of atmospheric lidar observations: some comments, Appl. Opt., 23, 652–653,
1028 doi.org/10.1364/AO.23.000652, 1984.
1029

1030 Flamant, P., Dabas, A., Martinet, P., Lever, V., Flament, T., Trapon, D., Olivier, M., Cuesta, J., and
1031 Huber, D.: Aeolus L2A Algorithm Theoretical Baseline Document, Particle optical properties
1032 product, version 5.7, available at: [https://earth.esa.int/eogateway/
1033 catalog/aeolus-l2a-aerosol-cloud-optical-product](https://earth.esa.int/eogateway/catalog/aeolus-l2a-aerosol-cloud-optical-product) (last access: 14 December 2021), 2021.
1034

1035 Flament, T., Trapon, D., Lacour, A., Dabas, A., Ehlers, F., and Huber, D.: Aeolus L2A aerosol optical
1036 properties product: standard correct algorithm and Mie correct algorithm, Atmos. Meas. Tech., 14,
1037 7851–7871, <https://doi.org/10.5194/amt-14-7851-2021>, 2021.
1038

1039 Fountoulakis, I., Papachristopoulou, K., Proestakis, E., Gkikas, A., Ioannis Raptis, P., Siomos, N.,
1040 Kontoes, C., and Kazadzis, S.: Effect of aerosol vertical distribution on the transfer of solar radiation
1041 through the atmosphere, EGU21-6111, <https://doi.org/10.5194/egusphere-egu21-6111>, 2021.
1042

1043 Freudenthaler, V.: About the effects of polarising optics on lidar signals and the $\Delta 90$ calibration,
1044 Atmos. Meas. Tech., 9, 4181–4255, <https://doi.org/10.5194/amt-9-4181-2016>, 2016.
1045

1046 Freudenthaler, V., Linné, H., Chaikovski, A., Rabus, D., Groß, S.: EARLINET lidar quality assurance
1047 tools, Atmos. Chem. Phys. Discuss., <https://doi.org/10.5194/amt-2017-395>, 2018.
1048

1049 Gelaro, R., McCarty, W., Suárez, M. J., Todling, R., Molod, A., Takacs, L., Randles, C. A., Darmenov,
1050 A., Bosilovich, M. G., Reichle, R., Wargan, K., Coy, L., Cullather, R., Draper, C., Akella, S.,
1051 Buchard, V., Conaty, A., da Silva, A. M., Gu, W., Kim, G., Koster, R., Lucchesi, R., Merkova, D.,
1052 Nielsen, J. E., Partyka, G., Pawson, S., Putman, W., Rienecker, M., Schubert, S. D., Sienkiewicz, M.,
1053 and Zhao, B.: The Modern-Era Retrospective Analysis for Research and Applications, Version 2
1054 (MERRA-2), *J. Climate*, 30, 5419–5454, <https://doi.org/10.1175/JCLI-D-16-0758.1>, 2017.
1055

1056 Gerasopoulos, E., Andreae, M. O., Zerefos, C. S., Andreae, T. W., Balis, D., Formenti, P., Merlet, P.,
1057 Amiridis, V., and Papastefanou, C.: Climatological aspects of aerosol optical properties in Northern
1058 Greece, *Atmos. Chem. Phys.*, 3, 2025–2041, <https://doi.org/10.5194/acp-3-2025-2003>, 2003.
1059

1060 Gerasopoulos, E., Amiridis, V., Kazadzis, S., Kokkalis, P., Eleftheratos, K., Andreae, M. O., Andreae,
1061 T. W., El-Askary, H., and Zerefos, C. S.: Three-year ground based measurements of aerosol optical
1062 depth over the Eastern Mediterranean: the urban environment of Athens, *Atmos. Chem. Phys.*, 11,
1063 2145–2159, <https://doi.org/10.5194/acp-11-2145-2011>, 2011.
1064

1065 Gialitaki, A., Tsekeri, A., Amiridis, V., Ceolato, R., Paulien, L., Kampouri, A., Gkikas, A., Solomos,
1066 S., Marinou, E., Haarig, M., Baars, H., Ansmann, A., Lapyonok, T., Lopatin, A., Dubovik, O., Groß,
1067 S., Wirth, M., Tschla, M., Tsikoudi, I., and Balis, D.: Is the near-spherical shape the “new black” for
1068 smoke?, *Atmos. Chem. Phys.*, 20, 14005–14021, <https://doi.org/10.5194/acp-20-14005-2020>, 2020.
1069

1070 Giles, D. M., Sinyuk, A., Sorokin, M. G., Schafer, J. S., Smirnov, A., Slutsker, I., Eck, T. F., Holben,
1071 B. N., Lewis, J. R., Campbell, J. R., Welton, E. J., Korkin, S. V., and Lyapustin, A. I.: Advancements
1072 in the Aerosol Robotic Network (AERONET) Version 3 database – automated near-real-time quality
1073 control algorithm with improved cloud screening for Sun photometer aerosol optical depth (AOD)
1074 measurements, *Atmos. Meas. Tech.*, 12, 169–209, <https://doi.org/10.5194/amt-12-169-2019>, 2019.
1075

1076 Gkikas, A., Hatzianastassiou, N., Mihalopoulos, N., Katsoulis, V., Kazadzis, S., Pey, J., Querol, X.,
1077 and Torres, O.: The regime of intense desert dust episodes in the Mediterranean based on
1078 contemporary satellite observations and ground measurements, *Atmos. Chem. Phys.*, 13, 12135–
1079 12154, <https://doi.org/10.5194/acp-13-12135-2013>, 2013.
1080

1081 Gkikas, A., Houssos, E. E., Lolis, C. J., Bartzokas, A., Mihalopoulos, N., and Hatzianastassiou, N.:
1082 Atmospheric circulation evolution related to desert-dust episodes over the Mediterranean, *Q. J. Roy.*
1083 *Meteor. Soc.*, 141, 1634–1645, <https://doi.org/10.1002/qj.2466>, 2015.

1084

1085 Gkikas, A., Basart, S., Hatzianastassiou, N., Marinou, E., Amiridis, V., Kazadzis, S., Pey, J., Querol,
1086 X., Jorba, O., Gassó, S., and Baldasano, J. M.: Mediterranean intense desert dust outbreaks and their
1087 vertical structure based on remote sensing data, *Atmos. Chem. Phys.*, 16, 8609–8642,
1088 <https://doi.org/10.5194/acp-16-8609-2016>, 2016.

1089

1090 Gkikas, A., Obiso, V., Pérez García-Pando, C., Jorba, O., Hatzianastassiou, N., Vendrell, L., Basart,
1091 S., Solomos, S., Gassó, S., and Baldasano, J. M.: Direct radiative effects during intense Mediterranean
1092 desert dust outbreaks, *Atmos. Chem. Phys.*, 18, 8757–8787, [https://doi.org/10.5194/acp-18-8757-](https://doi.org/10.5194/acp-18-8757-2018)
1093 [2018](https://doi.org/10.5194/acp-18-8757-2018), 2018.

1094

1095 Gkikas, A., Proestakis, E., Amiridis, V., Kazadzis, S., Di Tomaso, E., Marinou, E., Hatzianastassiou,
1096 N., Kok, J. F., and García-Pando, C. P.: Quantification of the dust optical depth across spatiotemporal
1097 scales with the MIDAS global dataset (2003–2017), *Atmos. Chem. Phys.*, 22, 3553–3578,
1098 <https://doi.org/10.5194/acp-22-3553-2022>, 2022.

1099

1100 Gueymard, C. A. and Yang, D.: Worldwide validation of CAMS and MERRA-2 reanalysis aerosol
1101 optical depth products using 15 years of AERONET observations, *Atmos. Environ.*, 225, 117216,
1102 <https://doi.org/10.1016/j.atmosenv.2019.117216>, 2020.

1103

1104 Haywood, J. M., Abel, S. J., Barrett, P. A., Bellouin, N., Blyth, A., Bower, K. N., Brooks, M.,
1105 Carslaw, K., Che, H., Coe, H., Cotterell, M. I., Crawford, I., Cui, Z., Davies, N., Dingley, B., Field,
1106 P., Formenti, P., Gordon, H., de Graaf, M., Herbert, R., Johnson, B., Jones, A. C., Langridge, J. M.,
1107 Malavelle, F., Partridge, D. G., Peers, F., Redemann, J., Stier, P., Szpek, K., Taylor, J. W., Watson-
1108 Parris, D., Wood, R., Wu, H., and Zuidema, P.: The CLOUD–Aerosol–Radiation Interaction and
1109 Forcing: Year 2017 (CLARIFY-2017) measurement campaign, *Atmos. Chem. Phys.*, 21, 1049–1084,
1110 <https://doi.org/10.5194/acp-21-1049-2021>, 2021.

1111

1112 Health Effects Institute, 2019, State of Global Air 2019, Special Report, Boston, MA: Health Effects
1113 Institute, ISSN 2578-6873,
1114 https://www.stateofglobalair.org/sites/default/files/soga_2019_report.pdf, 2019.

1115

1116 Horányi, A., Cardinali, C., Rennie, M., and Isaksen, L.: The assimilation of horizontal line-of-sight
1117 wind information into the ECMWF data assimilation and forecasting system. Part I: The assessment
1118 of wind impact, *Q. J. R. Meteorol. Soc.*, 141, 1223–1232, <https://doi.org/10.1002/qj.2430>, 2015a.

1119

1120 Horányi, A., Cardinali, C., Rennie, M., and Isaksen, L.: The assimilation of horizontal line-of-sight
1121 wind information into the ECMWF data assimilation and forecasting system. Part II: The impact of
1122 degraded wind observations, *Q. J. R. Meteorol. Soc.*, 141, 1233–1243,
1123 <https://doi.org/10.1002/qj.2551>, 2015b.

1124

1125 Illingworth, A. J., Barker, H. W., Beljaars, A., Ceccaldi, M., Chepfer, H., Clerbaux, N., Cole, J.,
1126 Delanoë, J., Domenech, C., Donovan, D. P., Fukuda, S., Hiraoka, M., Hogan, R. J., Huenerbein, A.,
1127 Kollias, P., Kubota, T., Nakajima, T., Nakajima, T. Y., Nishizawa, T., Ohno, Y., Okamoto, H., Oki,
1128 R., Sato, K., Satoh, M., Shephard, M. W., Velázquez-Blázquez, A., Wandinger, U., Wehr, T., and
1129 van Zadelhoff, G.-J.: The EarthCARE Satellite: The Next Step Forward in Global Measurements of
1130 Clouds, Aerosols, Precipitation, and Radiation, *Bull. Amer. Meteor. Soc.*, 96, 1311–1332,
1131 <https://doi.org/10.1175/BAMS-D-12-00227.1>, 2015.

1132

1133 Inness, A., Ades, M., Agustí-Panareda, A., Barré, J., Benedictow, A., Blechschmidt, A.-M.,
1134 Dominguez, J. J., Engelen, R., Eskes, H., Flemming, J., Huijnen, V., Jones, L., Kipling, Z., Massart,
1135 S., Parrington, M., Peuch, V.-H., Razinger, M., Remy, S., Schulz, M., and Suttie, M.: The CAMS
1136 reanalysis of atmospheric composition, *Atmos. Chem. Phys.*, 19, 3515–3556,
1137 <https://doi.org/10.5194/acp-19-3515-2019>, 2019.

1138

1139 Isaksen, L. and Rennie, M.: A preliminary evaluation of using Aeolus L2B Winds in ECMWF's NWP
1140 system, with focus on the tropical region, in: ESA Living Planet Symposium 2019, Milan, Italy,
1141 [https://lps19.esa.int/NikalWebsitePortal/living-planet-symposium-](https://lps19.esa.int/NikalWebsitePortal/living-planet-symposium-2019/lps19/Agenda/AgendaItemDetail?id=64570099-bea7-4b8f-a54b-5b6ad81fa342)
1142 [2019/lps19/Agenda/AgendaItemDetail?id=64570099-bea7-4b8f-a54b-5b6ad81fa342](https://lps19.esa.int/NikalWebsitePortal/living-planet-symposium-2019/lps19/Agenda/AgendaItemDetail?id=64570099-bea7-4b8f-a54b-5b6ad81fa342), last access: 8
1143 May 2020, 2019.

1144

1145 Jickells, T. D., An, Z. S., Andersen, K. K., Baker, A. R., Bergametti, G., Brooks, N., Cao, J. J., Boyd,
1146 P. W., Duce, R. A., Hunter, K. A., Kawahata, H., Kubilay, N., laRoche, J., Liss, P. S., Mahowald, N.,
1147 Prospero, J. M., Ridgwell, A. J., Tegen, I. and Torres, R.: Global Iron Connections Between Desert

1148 Dust, Ocean Biogeochemistry, and Climate, *Science*, 308(5718), 67–71,
1149 doi:10.1126/science.1105959, 2005.

1150

1151 Kampouri, A., Amiridis, V., Solomos, S., Gialitaki, A., Marinou, E., Spyrou, C., Georgoulas, A. K.,
1152 Akritidis, D., Papagiannopoulos, N., Mona, L., Scollo, S., Tschla, M., Tsikoudi, I., Pytharoulis, I.,
1153 Karacostas, T., and Zanis, P.: Investigation of Volcanic Emissions in the Mediterranean: “The Etna–
1154 Antikythera Connection,” *Atmos. Environ.*, 12, 40, <https://doi.org/10.3390/atmos12010040>, 2021.

1155

1156 Kanakidou, M., Mihalopoulos, N., Kindap, T., Im, U., Vrekoussis, M., Gerasopoulos, E., Dermizaki,
1157 E., Unal, A., Kocak, M., Markakis, K., Melas, D., Kouvarakis, G., Youssef, A. F., Richter, A.,
1158 Hatzianastassiou, N., Hilboll, A., Ebojie, F., Wittrock, F., von Savigny, C., Burrows, J. P.,
1159 Ladstaetter-Weissenmayer, A., and Moubasher, H.: Megacities as hot spots of air pollution in the East
1160 Mediterranean, *Atmos. Environ.*, 45, 1223–1235, <https://doi.org/10.1016/j.atmosenv.2010.11.048>,
1161 2011.

1162

1163 Kanitz, T., Lochard, J., Marshall, J., McGoldrick, P., Lecrenier, O., Bravetti, P., Reitebuch, O.,
1164 Rennie, M., Wernham, D., and Elfving, A.: Aeolus first light: first glimpse, in: International
1165 Conference on Space Optics – ICSO 2018, 9–12 October 2018, Chania, Greece, vol. 11180, 659–
1166 664, <https://doi.org/10.1117/12.2535982>, 2019.

1167

1168 Klett, J. D.: Stable analytical inversion solution for processing lidar returns, *Appl. Optics*, 20, 211–
1169 220, <https://doi.org/10.1364/AO.20.000211>, 1981.

1170

1171 Kosmopoulos, P. G., Kazadzis, S., El-Askary, H., Taylor, M., Gkikas, A., Proestakis, E., Kontoes, C.
1172 and El-Khayat, M. M.: Earth-Observation-Based Estimation and Forecasting of Particulate Matter
1173 Impact on Solar Energy in Egypt, *Remote Sens.*, 10(12), 1870, doi:10.3390/rs10121870, 2018.

1174

1175 Kosmopoulos, P.G., Kazadzis, S., Taylor, M., Raptis, P.I., Keramitsoglou, I., Kiranoudis, C., and
1176 Bais, A.F.: Assessment of the surface solar irradiance derived from real-time modelling techniques
1177 and verification with ground-based measurements. *Atmos. Meas. Tech.*, 11, pp 907-924, DOI:
1178 10.5194/amt-11-907-2018, 2018.

1179

1180 Lee, L., Zhang, J., Reid, J. S., and Yorks, J. E.: Investigation of CATS aerosol products and
1181 application toward global diurnal variation of aerosols, *Atmos. Chem. Phys.*, 19, 12687–12707,
1182 <https://doi.org/10.5194/acp-19-12687-2019>, 2019.

1183

1184 Lelieveld, J., Berresheim, H., Borrmann, S., Crutzen, P. J., Dentener, F. J., Fischer, H., Feichter, J.,
1185 Flatau, P. J., Heland, J., Holzinger, R., Korrman, R., Lawrence, M. G., Levin, Z., Markowicz, K.
1186 M., Mihalopoulos, N., Minikin, A., Ramanathan, V., de Reus, M., Roelofs, G. J., Scheeren, H. A.,
1187 Sciare, J., Schlager, H., Schultz, M., Siegmund, P., Steil, B., Stephanou, E. G., Stier, P., Traub, M.,
1188 Warneke, C., Williams, J., and Ziereis, H.: Global Air Pollution Crossroads over the Mediterranean,
1189 *Science*, 298, 794–799, <https://doi.org/10.1126/science.1075457>, 2002.

1190

1191 Lelieveld, J., Evans, J. S., Fnais, M., Giannadaki, D., and Pozzer, A.: The contribution of outdoor air
1192 pollution sources to premature mortality on a global scale, *Nature*, 525, 367–371,
1193 <https://doi.org/10.1038/nature15371>, 2015.

1194

1195 Levy, R. C., Mattoo, S., Munchak, L. A., Remer, L. A., Sayer, A. M., Patadia, F., and Hsu, N. C.:
1196 The Collection 6 MODIS aerosol products over land and ocean, *Atmos. Meas. Tech.*, 6, 2989–3034,
1197 <https://doi.org/10.5194/amt-6-2989-2013>, 2013.

1198

1199 Li, W., El-Askary, H., Qurban, M. A., Proestakis, E., Garay, M. J., Kalashnikova, O. V., Amiridis,
1200 V., Gkikas, A., Marinou, E., Piechota, T., and Manikandan, K. P.: An Assessment of Atmospheric
1201 and Meteorological Factors Regulating Red Sea Phytoplankton Growth, *Remote Sens.*, 10, 673,
1202 <https://doi.org/10.3390/rs10050673>, 2018.

1203

1204 Li, J., Carlson, B.E., Yung, Y.L. et al. Scattering and absorbing aerosols in the climate system. *Nat*
1205 *Rev Earth Environ* 3, 363–379 (2022). <https://doi.org/10.1038/s43017-022-00296-7>

1206

1207 Liu, D., Wang, Z., Liu, Z., Winker, D., and Trepte, C.: A height resolved global view of dust aerosols
1208 from the first year CALIPSO lidar measurements, *J. Geophys. Res.-Atmos.*, 113, D16214,
1209 <https://doi.org/10.1029/2007JD009776>, 2008.

1210

1211 Liu, Z., Kar, J., Zeng, S., Tackett, J., Vaughan, M., Avery, M., Pelon, J., Getzewich, B., Lee, K.-P.,
1212 Magill, B., Omar, A., Lucker, P., Trepte, C., and Winker, D.: Discriminating between clouds and

1213 aerosols in the CALIOP version 4.1 data products, *Atmos. Meas. Tech.*, 12, 703–734,
1214 <https://doi.org/10.5194/amt-12-703-2019>, 2019.
1215

1216 Lux, O., Lemmerz, C., Weiler, F., Marksteiner, U., Witschas, B., Rahm, S., Geiß, A., and Reitebuch,
1217 O.: Intercomparison of wind observations from the European Space Agency's Aeolus satellite mission
1218 and the ALADIN Airborne Demonstrator, *Atmos. Meas. Tech.*, 13, 2075–2097,
1219 <https://doi.org/10.5194/amt-13-2075-2020>, 2020.
1220

1221 Lux, O., Lemmerz, C., Weiler, F., Marksteiner, U., Witschas, B., Rahm, S., Geiß, A., Schäfler, A.,
1222 and Reitebuch, O.: Retrieval improvements for the ALADIN Airborne Demonstrator in support of
1223 the Aeolus wind product validation, *Atmos. Meas. Tech.*, 15, 1303–1331,
1224 <https://doi.org/10.5194/amt-15-1303-2022>, 2022.
1225

1226 Mallios, S. A., Daskalopoulou, V., and Amiridis, V.: Orientation of non spherical prolate dust
1227 particles moving vertically in the Earth's atmosphere, *J. Aerosol Sci.*, 151, 105657,
1228 doi:<https://doi.org/10.1016/j.jaerosci.2020.105657>, 2021.
1229

1230 Marinou, E., Amiridis, V., Biniotoglou, I., Tsikerdekis, A., Solomos, S., Proestakis, E., Konsta, D.,
1231 Papagiannopoulos, N., Tsekeri, A., Vlastou, G., Zanis, P., Balis, D., Wandinger, U. and Ansmann,
1232 A.: Three-dimensional evolution of Saharan dust transport towards Europe based on a 9-year
1233 EARLINET-optimized CALIPSO dataset, *Atmos. Chem. Phys.*, 17(9), 5893–5919, doi:10.5194/acp-
1234 17-5893-2017, 2017.
1235

1236 Martin, A., Weissmann, M., Reitebuch, O., Rennie, M., Geiß, A., and Cress, A.: Validation of Aeolus
1237 winds using radiosonde observations and numerical weather prediction model equivalents, *Atmos.*
1238 *Meas. Tech.*, 14, 2167–2183, <https://doi.org/10.5194/amt-14-2167-2021>, 2021.
1239

1240 Matthias, V., Freudenthaler, V., Amodeo, A., Balin, I., Balis, D., Bösenberg, J., Chaikovsky, A.,
1241 Chourdakis, G., Comeron, A., Delaval, A., De Tomasi, F., Eixmann, R., Hågård, A., Komguem, L.,
1242 Kreipl, S., Matthey, R., Rizi, V., Rodrigues, J., Wandinger, U., and Wang, X.: Aerosol lidar
1243 intercomparison in the framework of the EARLINET project. 1. Instruments, *Appl. Opt.*, 43, 961-
1244 976, doi:10.1364/AO.43.000961, 2004.
1245

1246 Mattis, I., D'Amico, G., Baars, H., Amodeo, A., Madonna, F., and Iarlori, M.: EARLINET Single
1247 Calculus Chain – technical – Part 2: Calculation of optical products, *Atmos. Meas. Tech.*, 9, 3009–
1248 3029, <https://doi.org/10.5194/amt-9-3009-2016>, 2016.

1249

1250 McGill, M. J., Yorks, J. E., Scott, V. S., Kupchock, A. W., and Selmer, P. A.: The Cloud Aerosol
1251 Transport System (CATS): A technology demonstration on the International Space Station, *Proc.*
1252 *SPIE* 9612, Lidar Remote Sensing for Environmental Monitoring XV, 96120A,
1253 <https://doi.org/10.1117/12.2190841>, 2015.

1254

1255 MétéoFrance: Algorithm theoretical basis document for cloud products (CMa-PGE01 v3.2, CT-
1256 PGE02 v2.2 & CTTH-PGE03 v2.2), Technical Report SAF/NWC/CDOP/MFL/SCI/ATBD/01,
1257 Paris: MétéoFrance, 2013.

1258

1259 Middleton, N., Tozer, P., and Tozer, B.: Sand and dust storms: underrated natural hazards, *Disasters*,
1260 43, 390–409, <https://doi.org/10.1111/disa.12320>, 2018.

1261

1262 Mishchenko, M. I. and Hovenier, J. W.: Depolarization of light backscattered by randomly oriented
1263 nonspherical particles, *Opt. Lett.*, 20(12), 1356, doi:10.1364/OL.20.001356, 1995.

1264

1265 Müller, D., Ansmann, A., Mattis, I., Tesche, M., Wandinger, U., Althausen, D., & Pisani, G. (2007).
1266 Aerosol-type-dependent lidar ratios observed with raman lidar. *Journal of Geophysical Research*
1267 *Atmospheres*, 112(16) doi:10.1029/2006JD008292

1268

1269 Okin, G. S., Mahowald, N., Chadwick, O. A. and Artaxo, P.: Impact of desert dust on the
1270 biogeochemistry of phosphorus in terrestrial ecosystems, *Global Biogeochemical Cycles*, 18(2),
1271 doi:10.1029/2003GB002145, 2004.

1272

1273 O'Neill, N. T., Eck, T. F., Smirnov, A., Holben, B. N., and Thulasiraman, S.: Spectral discrimination
1274 of coarse and fine mode optical depth, *J. Geophys. Res.*, 108, 4559–4573,
1275 <https://doi.org/10.1029/2002JD002975>, 2003.

1276

1277 Papagiannopoulos, N., D'Amico, G., Gialitaki, A., Ajtai, N., Alados-Arboledas, L., Amodeo, A.,
1278 Amiridis, V., Baars, H., Balis, D., Biniotoglou, I., Comerón, A., Dionisi, D., Falconieri, A., Fréville,
1279 P., Kampouri, A., Mattis, I., Mijić, Z., Molero, F., Papayannis, A., Pappalardo, G., Rodríguez-Gómez,

1280 A., Solomos, S. and Mona, L.: An EARLINET early warning system for atmospheric aerosol aviation
1281 hazards, *Atmospheric Chemistry and Physics*, 20(18), 10775–10789, doi:[https://doi.org/10.5194/acp-](https://doi.org/10.5194/acp-20-10775-2020)
1282 20-10775-2020, 2020.

1283

1284 Pappalardo, G., Amodeo, A., Apituley, A., Comeron, A., Freudenthaler, V., Linné, H., Ansmann, A.,
1285 Bösenberg, J., D'Amico, G., Mattis, I., Mona, L., Wandinger, U., Amiridis, V., Alados-Arboledas,
1286 L., Nicolae, D., and Wiegner, M.: EARLINET: towards an advanced sustainable European aerosol
1287 lidar network, *Atmos. Meas. Tech.*, 7, 2389–2409, <https://doi.org/10.5194/amt-7-2389-2014>, 2014.

1288

1289 Papayannis, A., Balis, D., Amiridis, V., Chourdakis, G., Tsaknakis, G., Zerefos, C., Castanho, A. D.
1290 A., Nickovic, S., Kazadzis, S., and Grabowski, J.: Measurements of Saharan dust aerosols over the
1291 Eastern Mediterranean using elastic backscatter-Raman lidar, spectrophotometric and satellite
1292 observations in the frame of the EARLINET project, *Atmos. Chem. Phys.*, 5, 2065–2079,
1293 <https://doi.org/10.5194/acp-5-2065-2005>, 2005.

1294

1295 Paschou, P., Siomos, N., Tsekeri, A., Louridas, A., Georgoussis, G., Freudenthaler, V., Biniotoglou,
1296 I., Tsaknakis, G., Tavernarakis, A., Evangelatos, C., von Bismarck, J., Kanitz, T., Meleti, C.,
1297 Marinou, E., and Amiridis, V.: The eVe reference polarisation lidar system for Cal/Val of Aeolus
1298 L2A product, *Atmos. Meas. Tech. Discuss.* [preprint], <https://doi.org/10.5194/amt-2021-268>, in
1299 review, 2021.

1300

1301 Pappalardo, G., Wandinger, U., Mona, L., Hiebsch, A., Mattis, I., Amodeo, A., Ansmann, A., Seifert,
1302 P., Linne, H., Apituley, A., Alados Arboledas, L., Balis, D., Chaikovsky, A., D'Amico, G., De
1303 Tomasi, F., Freudenthaler, V., Giannakaki, E., Giunta, A., Grigorov, I., Iarlori, M., Madonna, F.,
1304 Mamouri, R.-E., Nasti, L., Papayannis, A., Pietruczuk, A., Pujadas, M., Rizi, V., Rocadenbosch, F.,
1305 Russo, F., Schnell, F., Spinelli, N., Wang, X., and Wiegner, M.: EARLINET correlative
1306 measurements for CALIPSO: First intercomparison results, *J. Geophys. Res.*, 115, D00H19,
1307 doi:10.1029/2009JD012147, 2010.

1308

1309 Pappalardo, G., Amodeo, A., Apituley, A., Comeron, A., Freudenthaler, V., Linné, H., Ansmann, A.,
1310 Bösenberg, J., D'Amico, G., Mattis, I., Mona, L., Wandinger, U., Amiridis, V., Alados-Arboledas,
1311 L., Nicolae, D., and Wiegner, M.: EARLINET: towards an advanced sustainable European aerosol
1312 lidar network, *Atmos. Meas. Tech.*, 7, 2389–2409, <https://doi.org/10.5194/amt-7-2389-2014>, 2014.

1313

1314 Pérez, C., Nickovic, S., Pejanovic, G., Baldasano, J. M., and Özsoy, E.: Interactive dust-radiation
1315 modeling: A step to improve weather forecasts, *J. Geophys. Res.*, 111, 1–17, 2006.
1316

1317 Pisso, I., Sollum, E., Grythe, H., Kristiansen, N.I., Cassiani, M., Eckhardt, S., Arnold, D., Morton,
1318 D., Thompson, R.L., Groot Zwaafink, C.D., Evangeliou, N., Sodemann, H., Haimberger, L., Henne,
1319 S., Brunner, D., Burkhart, J.F., Fouilloux, A., Brioude, J., Philipp, A., Seibert, P., and Stohl, A.:
1320 FLEXPART 10.4 (Version 10.4), *Geosci. Model Dev. Discuss.* Zenodo,
1321 <https://doi.org/10.5281/zenodo.3542278>, 2019.
1322

1323 Pöschl, U.: Atmospheric Aerosols: Composition, Transformation, Climate and Health Effects,
1324 *ANGEW CHEM INT EDIT*, 44, 7520-7540, 10.1002/anie.200501122, 2005.
1325

1326 Proestakis, E., Amiridis, V., Marinou, E., Georgoulas, A. K., Solomos, S., Kazadzis, S., Chimot, J.,
1327 Che, H., Alexandri, G., Biniotoglou, I., Daskalopoulou, V., Kourtidis, K. A., de Leeuw, G. and
1328 Ronald, J. van der A.: Nine-year spatial and temporal evolution of desert dust aerosols over South
1329 and East Asia as revealed by CALIOP, *Atmos. Chem. Phys.*, 18(2), 1337–1362, doi:10.5194/acp-18-
1330 1337-2018, 2018.
1331

1332 Proestakis, E., Amiridis, V., Marinou, E., Biniotoglou, I., Ansmann, A., Wandinger, U., Hofer, J.,
1333 Yorks, J., Nowotnick, E., Makhmudov, A., Papayannis, A., Pietruczuk, A., Gialitaki, A., Apituley,
1334 A., Szkop, A., Muñoz Porcar, C., Bortoli, D., Dionisi, D., Althausen, D., Mamali, D., Balis, D.,
1335 Nicolae, D., Tetoni, E., Liberti, G. L., Baars, H., Mattis, I., Stachlewska, I. S., Voudouri, K. A., Mona,
1336 L., Mylonaki, M., Perrone, M. R., Costa, M. J., Sicard, M., Papagiannopoulos, N., Siomos, N.,
1337 Burlizzi, P., Pauly, R., Engelmann, R., Abdullaev, S., and Pappalardo, G.: EARLINET evaluation of
1338 the CATS Level 2 aerosol backscatter coefficient product, *Atmos. Chem. Phys.*, 19, 11743–11764,
1339 <https://doi.org/10.5194/acp-19-11743-2019>, 2019.
1340

1341 Pye, H.O.T., Ward-Caviness, C.K., Murphy, B.N. et al. Secondary organic aerosol association with
1342 cardiorespiratory disease mortality in the United States. *Nat Commun* 12, 7215 (2021).
1343 <https://doi.org/10.1038/s41467-021-27484-1>
1344

1345 Randles, C. A., da Silva, A. M., Buchard, V., Colarco, P. R., Darmenov, A., Govindaraju, R.,
1346 Smirnov, A., Holben, B., Ferrare, R., Hair, J., Shinozuka, Y., Flynn, C. J., Randles, C. A., Silva, A.
1347 M. da, Buchard, V., Colarco, P. R., Darmenov, A., Govindaraju, R., Smirnov, A., Holben, B., Ferrare,

1348 R., Hair, J., Shinozuka, Y., and Flynn, C. J.: The MERRA-2 Aerosol Reanalysis, 1980 Onward. Part
1349 I: System Description and Data Assimilation Evaluation, *J. Climate*, 30, 6823–6850,
1350 <https://doi.org/10.1175/JCLI-D-16-0609.1>, 2017.

1351

1352 Reitebuch, O., Lemmerz, C., Lux, O., Marksteiner, U., Rahm, S., Weiler, F., Witschas, B., Meringer,
1353 M., Schmidt, K., Huber, D., Nikolaus, I., Geiss, A., Vaughan, M., Dabas, A., Flament, T., Stieglitz,
1354 H., Isaksen, L., Rennie, M., de Kloe, J., Marseille, G.-J., Stoffelen, A., Wernham, D., Kanitz, T.,
1355 Straume, A.-G., Fehr, T., von Bismarck, J., Floberghagen, R., and Parrinello, T.: Initial Assessment
1356 of the Performance of the First Wind Lidar in Space on Aeolus, *EPJ Web Conf.*, 237, 01010,
1357 <https://doi.org/10.1051/epjconf/202023701010>, 2020.

1358

1359 Remer, L. A., Kleidman, R. G., Levy, R. C., Kaufman, Y. J., Tanré, D., Mattoo, S., Martins, J. V.,
1360 Ichoku, C., Koren, I., Yu, H. and Holben, B. N.: Global aerosol climatology from the MODIS satellite
1361 sensors, *J. Geophys. Res.-Atmos.*, 113, D14S07, <https://doi.org/10.1029/2007JD009661>, 2008.

1362

1363 Rennie, M. P. and Isaksen, L.: Investigations Into the Quality of Aeolus L2B Winds Using the
1364 ECMWF Model and Initial NWP Impact Assessment, in: *ESA Living Planet Symposium 2019*,
1365 Milan, Italy, [https://lps19.esa.int/NikalWebsitePortal/living-planet-symposium-](https://lps19.esa.int/NikalWebsitePortal/living-planet-symposium-2019/lps19/Agenda/AgendaItemDetail?id=1a3d272c-f7d1-4847-b1c4-08c452f9405f)
1366 [2019/lps19/Agenda/AgendaItemDetail?id=1a3d272c-f7d1-4847-b1c4-08c452f9405f](https://lps19.esa.int/NikalWebsitePortal/living-planet-symposium-2019/lps19/Agenda/AgendaItemDetail?id=1a3d272c-f7d1-4847-b1c4-08c452f9405f), last access: 8
1367 May 2020, 2019.

1368

1369 Rennie, M. P., Isaksen, L., Weiler, F., de Kloe, J., Kanitz, T., and Reitebuch, O.: The impact of Aeolus
1370 wind retrievals on ECMWF global weather forecasts, *Q. J. Roy. Meteor. Soc.*, 147, 3555–3586,
1371 <https://doi.org/10.1002/qj.4142>, 2021.

1372

1373 Richardson, S. C., Mytilinaios, M., Foskinis, R., Kyrou, C., Papayannis, A., Pyrri, I., Giannoutsou,
1374 E., and Adamakis, I. D. S.: Bioaerosol detection over Athens, Greece using the laser induced
1375 fluorescence technique, *Sci. Total Environ.*, 696, 133906,
1376 <https://doi.org/10.1016/j.scitotenv.2019.133906>, 2019.

1377

1378 Roebeling, R. A., Feijt, A. J., and Stamnes, P.: Cloud property retrievals for climate monitoring:
1379 implications of differences between SEVIRI on METEOSAT-8 and AVHRR on NOAA-17, *J.*
1380 *Geophys. Res.*, 111, 20210, <https://doi.org/10.1029/2005JD006990>, 2006.

1381

1382 Roy, G. and Roy, N.: Relation between circular and linear depolarization ratios under multiple-
1383 scattering conditions, *Appl. Opt.*, doi:10.1364/ao.47.006563, 2008.
1384

1385 Sasano, Y. and Nakane, H.: Significance of the extinction/backscatter ratio and the boundary value
1386 term in the solution for the two-component lidar equation, *Appl. Opt.*, 23(1), 11_1--13,
1387 doi:10.1364/AO.23.0011_1, 1984.
1388

1389 Sayer, A. M., Hsu, N. C., Bettenhausen, C., and Jeong, M.-J.: Validation and uncertainty estimates
1390 for MODIS Collection 6 “Deep Blue” aerosol data, *J. Geophys. Res.*, 118, 7864–7873,
1391 <https://doi.org/10.1002/jgrd.50600>, 2013.
1392

1393 Schmetz, J., Pili, P., Tjemkes, S., Just, D., Kerkmann, J., Rota, S., and Ratier, A.: An introduction to
1394 Meteosat Second Generation (MSG), *B. Am. Meteorol. Soc.*, 83, 977–992,
1395 [https://doi.org/10.1175/1520-0477\(2002\)083<0977:AITMSG>2.3.CO;2](https://doi.org/10.1175/1520-0477(2002)083<0977:AITMSG>2.3.CO;2), 2002.
1396

1397 Shinozuka, Y. and Redemann, J.: Horizontal variability of aerosol optical depth observed during the
1398 ARCTAS airborne experiment, *Atmos. Chem. Phys.*, 11, 8489–8495, [https://doi.org/10.5194/acp-11-](https://doi.org/10.5194/acp-11-8489-2011)
1399 [8489-2011](https://doi.org/10.5194/acp-11-8489-2011), 2011.
1400

1401 Sinyuk, A., Holben, B. N., Eck, T. F., Giles, D. M., Slutsker, I., Korokin, S., Schafer, J. S., Smirnov,
1402 A., Sorokin, M., and Lyapustin, A.: The AERONET Version 3 aerosol retrieval algorithm, associated
1403 uncertainties and comparisons to Version 2, *Atmos. Meas. Tech.*, 13, 3375–3411,
1404 <https://doi.org/10.5194/amt-13-3375-2020>, 2020.
1405

1406 Siomos, N., Balis, D. S., Voudouri, K. A., Giannakaki, E., Filioglou, M., Amiridis, V., Papayannis,
1407 A., and Fragkos, K.: Are EARLINET and AERONET climatologies consistent? The case of
1408 Thessaloniki, Greece, *Atmos. Chem. Phys.*, 18, 11885–11903, [https://doi.org/10.5194/acp-18-11885-](https://doi.org/10.5194/acp-18-11885-2018)
1409 [2018](https://doi.org/10.5194/acp-18-11885-2018), 2018.
1410

1411 Solomon S., Dube K., Stone K., Yu P., Kinnison D., Toon O.B., Strahan S.E., Rosenlof K.H.,
1412 Portmann R., Davis S., Randel W., Bernath P., Boone C., Bardeen C.G., Bourassa A., Zawada D.,
1413 Degenstein D.: On the stratospheric chemistry of midlatitude wildfire smoke (2022) *Proceedings of*
1414 *the National Academy of Sciences of the United States of America*, 119 (10), pp. e2117325119 DOI:
1415 10.1073/pnas.2117325119

1416

1417 Stoffelen, A., Pailleux, J., Källén, E., Vaughan, J. M., Isaksen, L., Flamant, P., Wergen, W.,
1418 Andersson, E., Schyberg, H., Culoma, A., Meynard, R., Endemann, M., and Ingmann, P.: The
1419 atmospheric dynamics mission for global wind field measurement, *B. Am. Meteorol. Soc.*, 86, 73-87,
1420 <https://doi.org/10.1175/BAMS-86-1-73>, 2005.

1421

1422 Stohl, A., Forster, C., Frank, A., Seibert, P., and Wotawa, G.: Technical note: The Lagrangian particle
1423 dispersion model FLEXPART version 6.2, *Atmos. Chem. Phys.*, 5, 2461–2474, doi:10.5194/acp-5-
1424 2461-2005, 2005.

1425

1426 Straume, A.G., Schuettmeyer, D., von Bismarck, J., Kanitz, T., Fehr, T., EOP-SM/2945/AGS-ags,
1427 PL-Plan, European Space Agency (ESA),
1428 [https://earth.esa.int/eogateway/documents/20142/1564626/Aeolus-Scientific-CAL-VAL-
1429 Implementation-Plan.pdf](https://earth.esa.int/eogateway/documents/20142/1564626/Aeolus-Scientific-CAL-VAL-Implementation-Plan.pdf), 2019.

1430

1431 Straume, A. G., Rennie, M., Isaksen, L., de Kloe, J., Marseille, G.-J., Stoffelen, A., Flament, T.,
1432 Stieglitz, H., Dabas, A., Huber, D., Reitebuch, O., Lemmerz, C., Lux, O., Marksteiner, U., Weiler,
1433 F., Witschas, B., Meringer, M., Schmidt, K., Nikolaus, I., Geiß, A., Flamant, P., Kanitz, T., Wernham,
1434 D., von Bismarck, J., Bley, S., Fehr, T., Floberghagen, R., and Parrinello, T.: ESA's space-based
1435 Doppler wind lidar mission Aeolus – First wind and aerosol product assessment results, *EPJ Web
1436 Conf.*, 237, 01007, <https://doi.org/10.1051/epjconf/202023701007>, 2020.

1437

1438 Tyrllis, E. and Lelieveld, J.: Climatology and Dynamics of the Summer Etesian Winds over the
1439 Eastern Mediterranean, *J. Atmos. Sci.*, 70, 3374–3396, 2013.

1440

1441 van der Werf, G. R., Randerson, J. T., Giglio, L., van Leeuwen, T. T., Chen, Y., Rogers, B. M., Mu,
1442 M., van Marle, M. J. E., Morton, D. C., Collatz, G. J., Yokelson, R. J., and Kasibhatla, P. S.: Global
1443 fire emissions estimates during 1997–2016, *Earth Syst. Sci. Data*, 9, 697–720,
1444 <https://doi.org/10.5194/essd-9-697-2017>, 2017.

1445

1446 Ulanowski, Z., Bailey, J., Lucas, P. W., Hough, J. H., and Hirst, E.: Alignment of atmospheric mineral
1447 dust due to electric field, *Atmos. Chem. Phys.*, 7, 6161–6173, [https://doi.org/10.5194/acp-7-6161-
1448 2007](https://doi.org/10.5194/acp-7-6161-2007), 2007.

1449

1450 Varlas, G.; Marinou, E.; Gialitaki, A.; Siomos, N.; Tsarpalis, K.; Kalivitis, N.; Solomos, S.; Tsekeri,
1451 A.; Spyrou, C.; Tsihla, M.; Kampouri, A.; Vervatis, V.; Giannakaki, E.; Amiridis, V.; Mihalopoulos,
1452 N.; Papadopoulos, A.; Katsafados, P. Assessing Sea-State Effects on Sea-Salt Aerosol Modeling in
1453 the Lower Atmosphere Using Lidar and In-Situ Measurements. *Remote Sens.*, 13, 614.
1454 <https://doi.org/10.3390/rs13040614>, 2021.

1455

1456 Voudouri, K.A., Siomos, N., Michailidis, K., D'Amico, G., Mattis, I., Balis, D.: Consistency of the
1457 Single Calculus Chain optical products with archived measurements from an EARLINET lidar
1458 station, *Remote Sensing*. 2020; 12(23):3969. <https://doi.org/10.3390/rs12233969>, 2020.

1459

1460 Wei, J., Li, Z., Peng, Y., and Sun, L.: MODIS Collection 6.1 aerosol optical depth products over land
1461 and ocean: validation and comparison, *Atmos. Environ.*, 201, 428–440, 2019

1462

1463 Weiler, F., Rennie, M., Kanitz, T., Isaksen, L., Checa, E., de Kloe, J., Okunde, N., and Reitebuch, O.:
1464 Correction of wind bias for the lidar on board Aeolus using telescope temperatures, *Atmos. Meas.
1465 Tech.*, 14, 7167–7185, <https://doi.org/10.5194/amt-14-7167-2021>, 2021.

1466

1467 Weinzierl, B., Ansmann, A., Prospero, J. M., Althausen, D., Benker, N., Chouza, F., Dollner, M.,
1468 Farrell, D., Fomba, W. K., Freudenthaler, V., Gasteiger, J., Groß, S., Haarig, M., Heinold, B.,
1469 Kandler, K., Kristensen, T. B., Mayol-Bracero, O. L., Müller, T., Reitebuch, O., Sauer, D., Schäfler,
1470 A., Schepanski, K., Spanu, A., Tegen, I., Toledano, C. and Walser, A.: The Saharan Aerosol Long-
1471 Range Transport and Aerosol–Cloud-Interaction Experiment: Overview and Selected Highlights,
1472 *Bull. Amer. Meteor. Soc.*, 98(7), 1427–1451, doi:10.1175/BAMS-D-15-00142.1, 2016.

1473

1474 Wilks, D.S. *Statistical Methods in the Atmospheric Sciences*, 4th ed.; Elsevier: Cambridge, MA,
1475 USA, 2019.

1476

1477 Winker, D. M., Vaughan, M. A., Omar, A., Hu, Y., Powell, K. A., Liu, Z., Hunt, W. H. and Young,
1478 S. A.: Overview of the CALIPSO Mission and CALIOP Data Processing Algorithms, *J. Atmos.
1479 Ocean. Technol.*, 26(11), 2310–2323, doi:10.1175/2009JTECHA1281.1, 2009.

1480

1481 Witschas, B., Lemmerz, C., Geiß, A., Lux, O., Marksteiner, U., Rahm, S., Reitebuch, O., and Weiler,
1482 F.: First validation of Aeolus wind observations by airborne Doppler wind lidar measurements,
1483 *Atmos. Meas. Tech.*, 13, 2381–2396, <https://doi.org/10.5194/amt-13-2381-2020>, 2020.

1484
1485
1486
1487
1488
1489
1490
1491
1492
1493
1494
1495
1496
1497
1498
1499
1500
1501
1502
1503
1504
1505
1506
1507
1508
1509
1510
1511
1512
1513
1514
1515
1516
1517
1518
1519
1520
1521

Witschas, B., Lemmerz, C., Lux, O., Marksteiner, U., Reitebuch, O., Weiler, F., Fabre, F., Dabas, A., Flament, T., Huber, D., and Vaughan, M.: Spectral performance analysis of the Aeolus Fabry–Pérot and Fizeau interferometers during the first years of operation, *Atmos. Meas. Tech.*, 15, 1465–1489, <https://doi.org/10.5194/amt-15-1465-2022>, 2022.

Zeng, S., Vaughan, M., Liu, Z., Trepte, C., Kar, J., Omar, A., Winker, D., Lucker, P., Hu, Y., Getzewich, B., and Avery, M.: Application of high-dimensional fuzzy *k*-means cluster analysis to CALIOP/CALIPSO version 4.1 cloud–aerosol discrimination, *Atmos. Meas. Tech.*, 12, 2261–2285, <https://doi.org/10.5194/amt-12-2261-2019>, 2019.

Zerefos, C., Nastos, P., Balis, D., Papayannis, A., Kelepertsis, A., Kanellopoulou, E., Nikolakis, D., Eleftheratos, C., Thomas, W., and Varotsos, C.: A complex study of Etna's volcanic plume from ground-based, in situ and space-borne observations, *International J. Remote Sens.*, 27, 1855–1864, <https://doi.org/10.1080/01431160500462154>, 2006.

1522 **Table 1:** Statistical metrics for the unfiltered (clouds plus aerosols) Aeolus L2A SCA and SCA mid-bin backscatter (in
 1523 $\text{Mm}^{-1}\text{sr}^{-1}$) profiles at each PANACEA site.

	SCA					SCA_mid_bin				
Station	Counts	Bias	Rel. Bias (%)	R	RMSE	Counts	Bias	Rel. Bias (%)	R	RMSE
ANT	255	0.06	13.63	0.49	1.14	173	0.25	45.59	0.57	1.01
ATH	60	0.73	199.65	0.49	2.26	43	1.16	272.84	0.52	3.10
THE	222	0.83	185.16	0.34	2.60	140	1.10	224.65	0.32	2.19

1524

1525 **Table 2:** As in Table 1 but for the filtered (only aerosols) Aeolus backscatter retrievals (in $\text{Mm}^{-1}\text{sr}^{-1}$).

	SCA					SCA_mid_bin				
Station	Counts	Bias	Rel. Bias (%)	R	RMSE	Counts	Bias	Rel. Bias (%)	R	RMSE
ANT	94	-0.10	-26.57	0.55	0.78	57	0.06	13.35	0.86	0.43
ATH	12	1.08	483.36	0.75	3.33	9	0.73	312.67	0.82	1.41
THE	133	0.46	130.49	0.39	1.86	81	0.55	145.08	0.43	1.20

1526

1527

1528

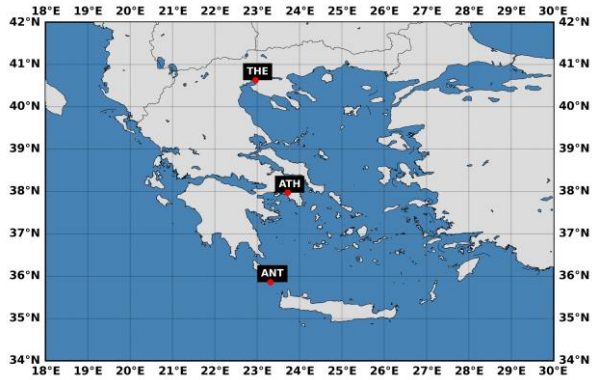
1529

1530

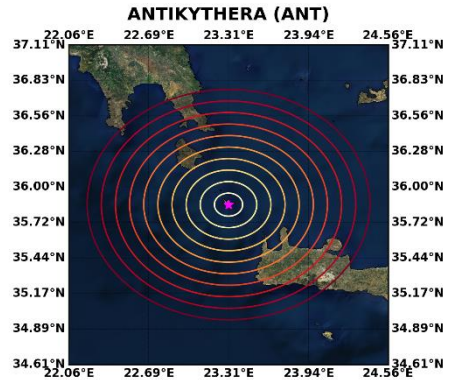
1531

1532

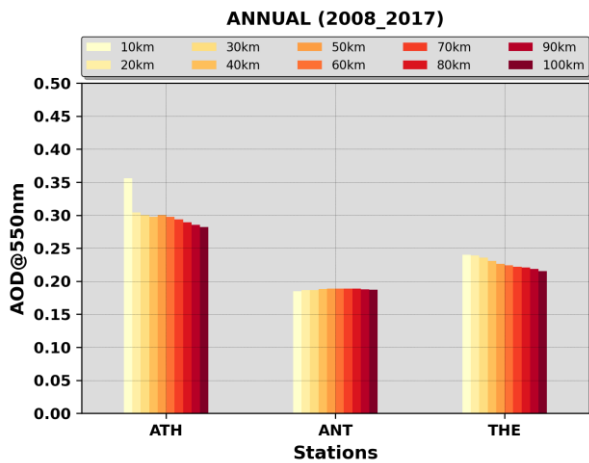
1533



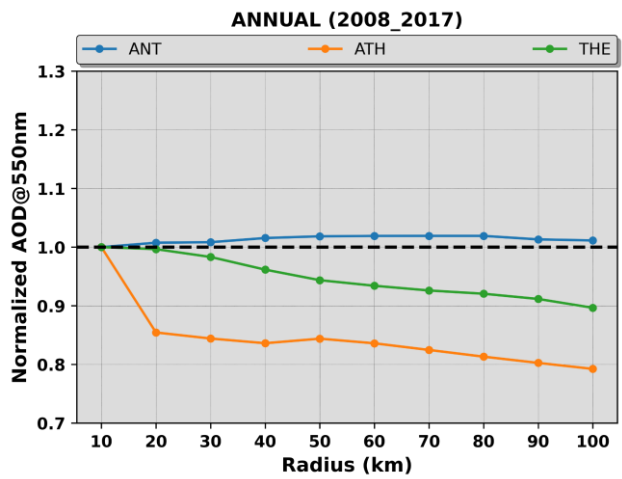
(i)



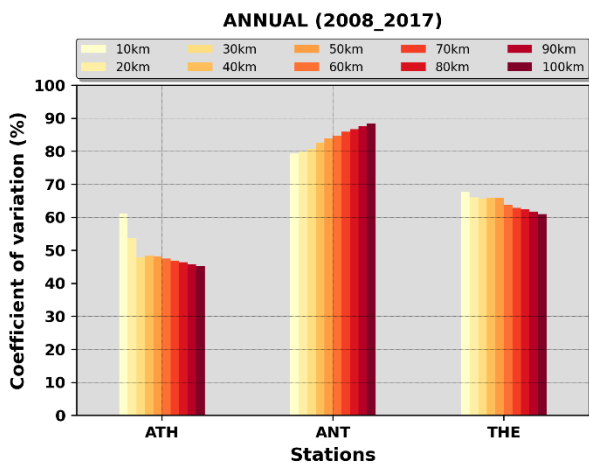
(ii)



(iii)

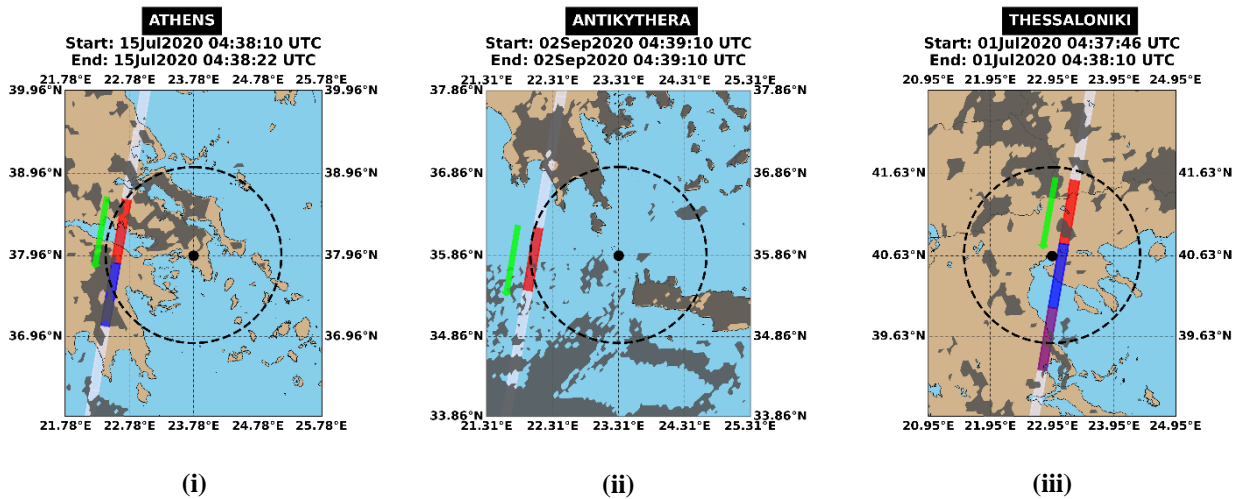


(iv)



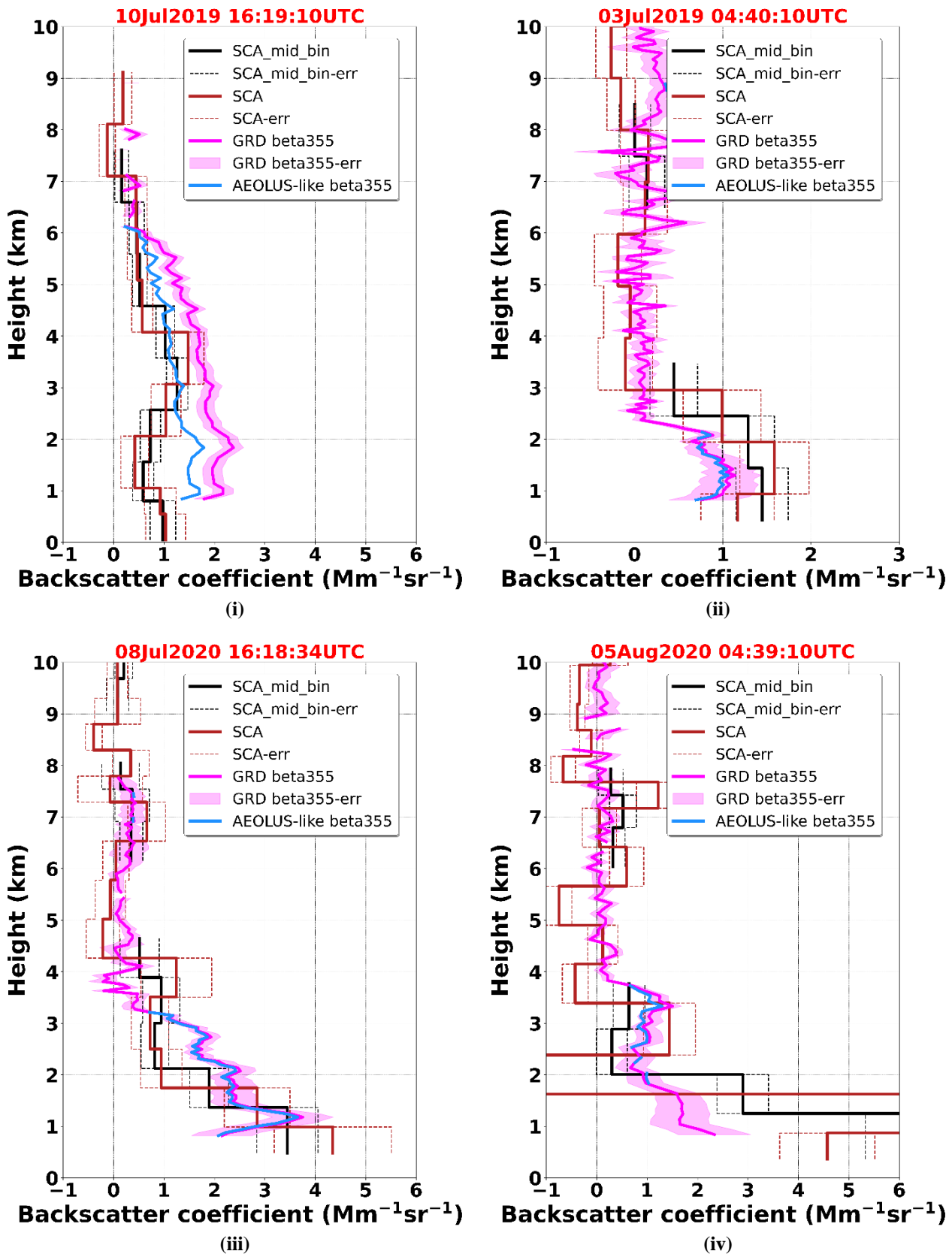
(v)

1534 **Figure 1:** (i) Locations of the three Greek PANACEA sites, namely Athens (ATH), Antikythera (ANT) and Thessaloniki
 1535 (THE), (ii) Concentric circles, around the Antikythera island, of radii from 10 to 100 km with an incremental step of 10
 1536 km, (iii) Climatological MODIS-Aqua AOD levels, representative for the period 2008 – 2017, for each circle area centered
 1537 at each PANACEA site, (iv) Normalized climatological AODs for each circle area with respect to the corresponding
 1538 levels of the inner circle.



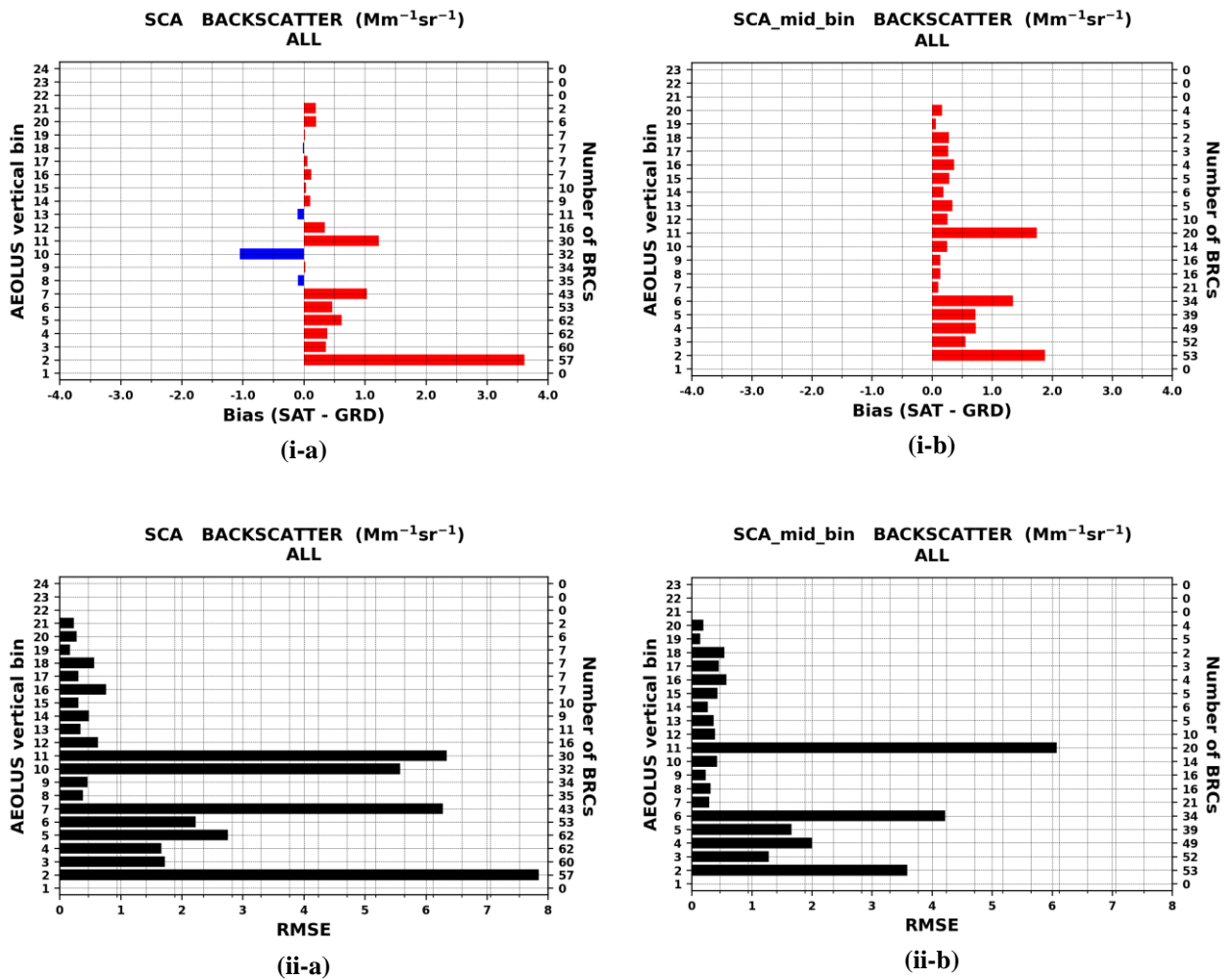
1539 **Figure 2:** The white stripe indicates the ALADIN's measurements track and the colored rectangles correspond to the
 1540 Aeolus observations (~90 km along-track averaged measurements) falling within a radius of 120 km (dashed black line)
 1541 of the PANACEA stations (black dot). The orange arrow shows the Aeolus flight directions (ascending or descending
 1542 orbit). Dark grey shaded areas: MSG-SEVIRI cloud mask product (CLM) at the nearest time to Aeolus overpass. The
 1543 start and end time (in UTC) of the ALADIN observations are given in the title of each plot.

1544
 1545
 1546
 1547
 1548
 1549
 1550
 1551
 1552
 1553
 1554
 1555
 1556
 1557
 1558
 1559
 1560
 1561
 1562
 1563
 1564



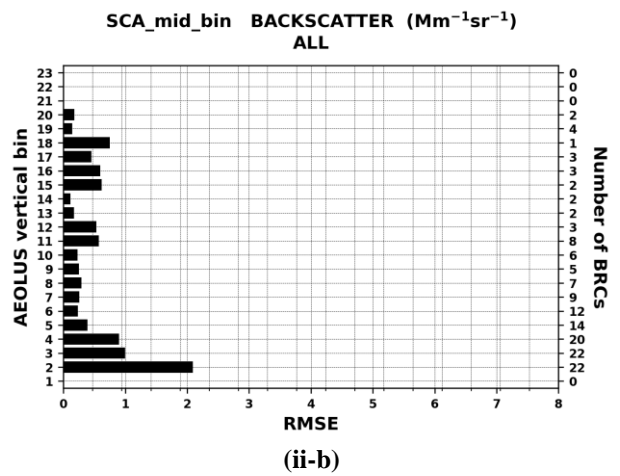
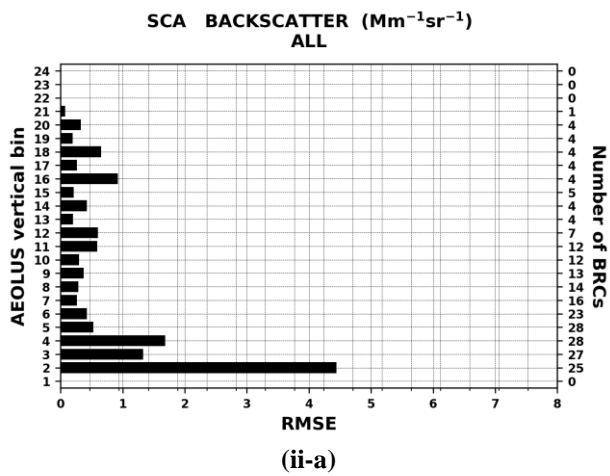
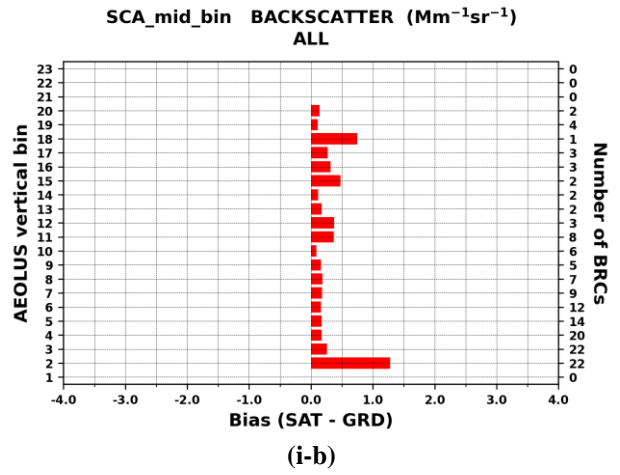
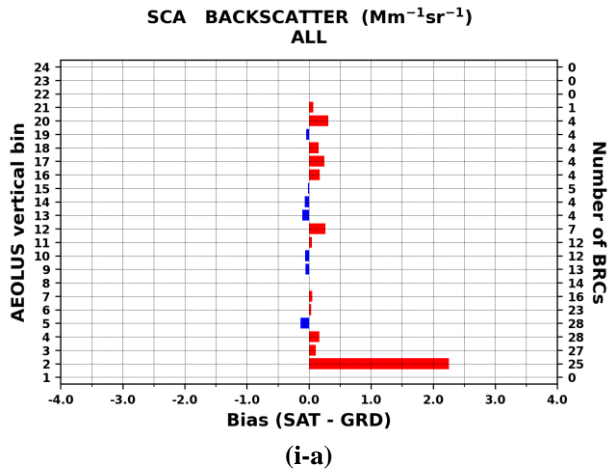
1565 **Figure 3:** Vertical profiles of backscatter coefficient at 355 nm acquired by ALADIN for the Level 2A SCA (regular
 1566 vertical observation grid, brown solid curve) and SCA mid-bin (reduced vertical observation grid, black solid curve)
 1567 products. The dashed lines correspond to the estimated SCA backscatter coefficient errors (brown) and SCA mid-bin
 1568 backscatter coefficient errors (black). Vertical profile of Polly^{XT} backscatter coefficient (pink solid curve) at UV
 1569 wavelength (355 nm) and associated errors (pink shaded area). Polly^{XT} Aeolus-like backscatter coefficient (light-blue

1570 solid curve) after converting the linear-derived products to circular co-polar according to Paschou et al. (2021). The
 1571 ground-based profiles have been acquired at the Antikythera station (southwest Greece) on: (i) 10th July 2019, (ii) 3rd July
 1572 2019, (iii) 8th July 2020 and (iv) 5th August 2020. The red color font denotes which Aeolus BRC (along with the overpass
 1573 time) has been selected based on the defined collocation criteria.
 1574



1575 **Figure 4:** Bias (i) and root mean square error (ii) metrics for the unfiltered Aeolus L2A backscatter retrievals reported at
 1576 the regular (a) and mid-bin (b) vertical scales. The biases are defined as SAT-GRD and the positive/negative departures
 1577 are depicted with red/blue bars. The statistical metrics are vertically resolved based on Aeolus bins indices (left y-axis).
 1578 The number of BRCs participating in the metrics calculations at each bin are given on the right y-axis.

1579
 1580
 1581
 1582
 1583
 1584
 1585
 1586
 1587



1588 **Figure 5:** As in Figure 4 but for the filtered Aeolus L2A backscatter retrievals.

1589

1590

1591

1592

1593

1594

1595

1596

1597

1598

1599

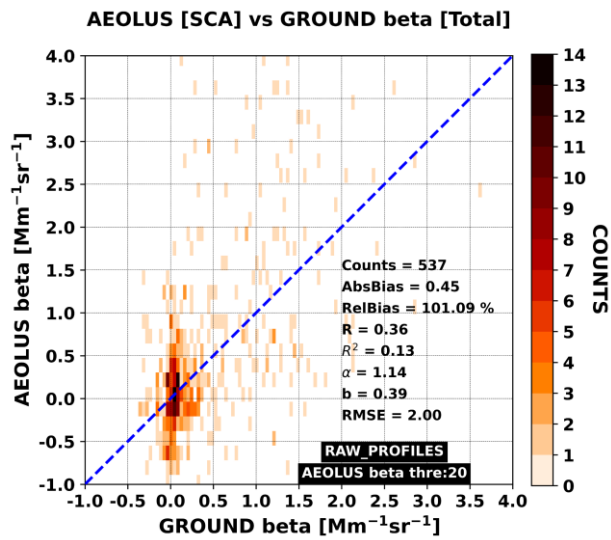
1600

1601

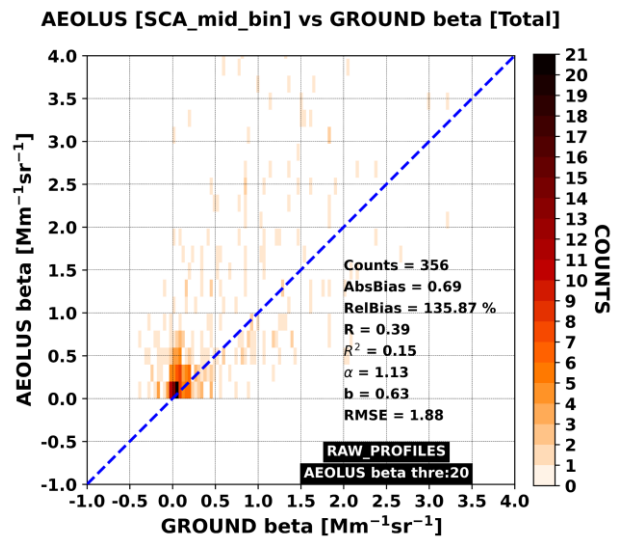
1602

1603

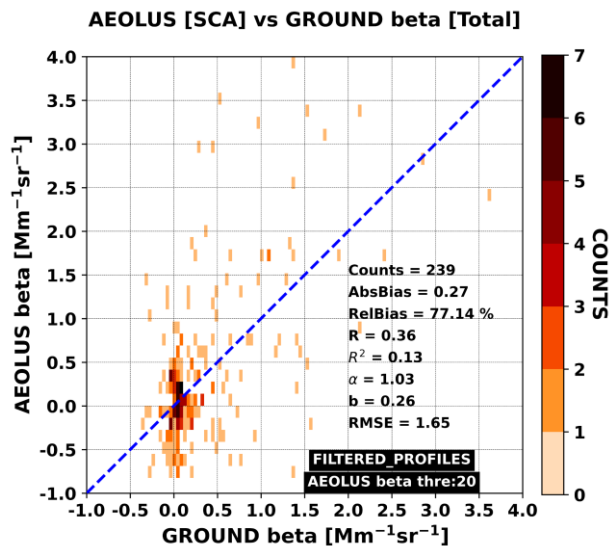
1604



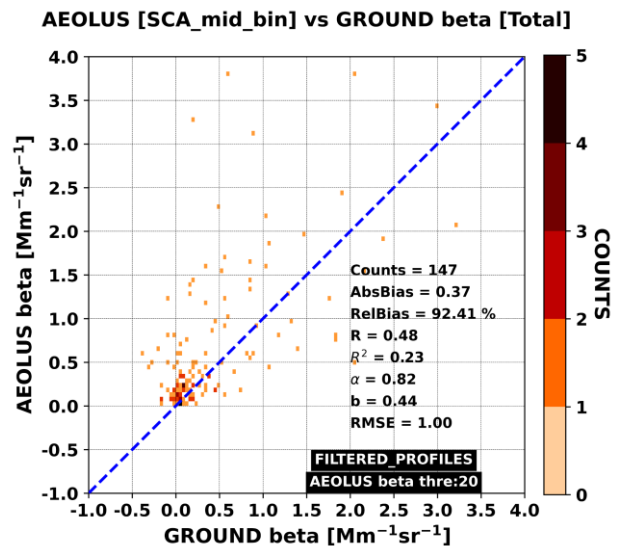
(i-a)



(i-b)



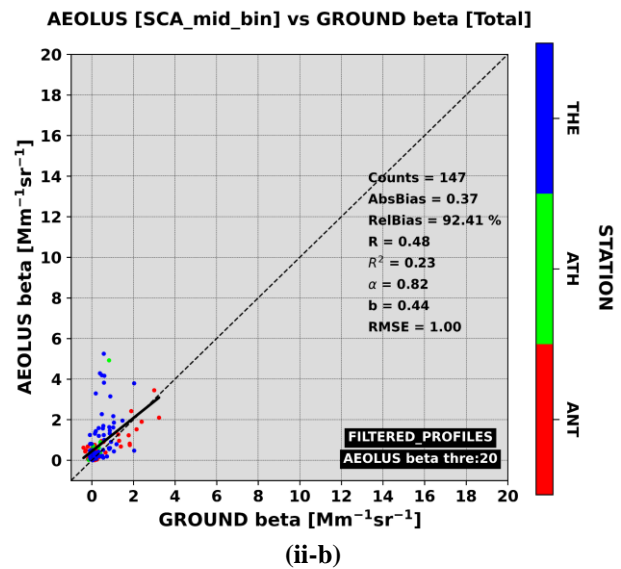
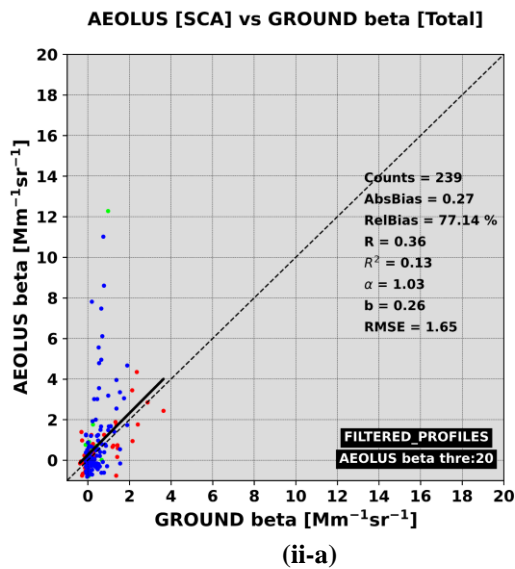
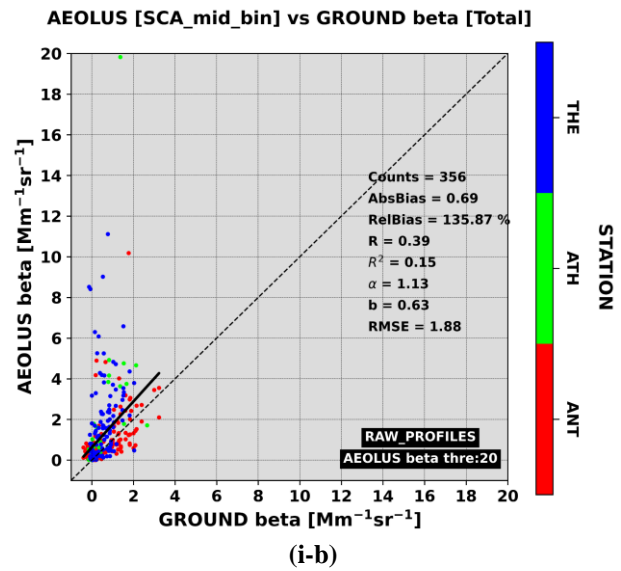
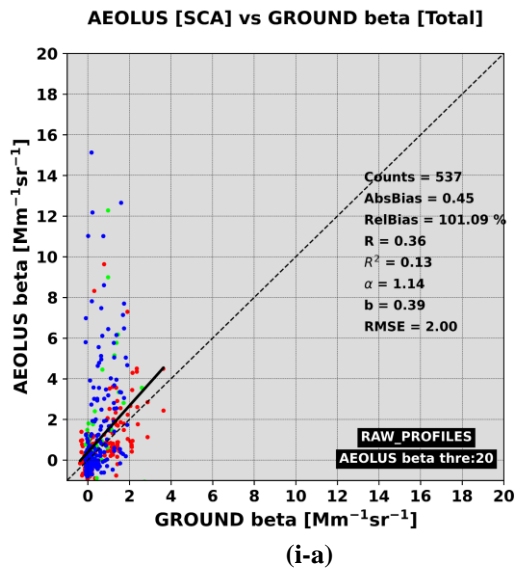
(ii-a)



(ii-b)

1605 **Figure 6:** 2D histograms between Aeolus (y-axis) and ground-based (x-axis) backscatter coefficient retrievals. In the
 1606 upper (i) and bottom (ii) panels are depicted the results for the cloud+aerosol backscatter (unfiltered) and cloud-cleared
 1607 backscatter (filtered) Aeolus profiles, respectively. On the left and right columns are illustrated the results corresponding
 1608 to Aeolus regular (24 bins) and mid-bin (23 bins) vertical scales, respectively. Aeolus backscatter values larger than 20
 1609 $\text{Mm}^{-1} \text{sr}^{-1}$ are masked out from the collocated sample.

1610
 1611
 1612
 1613



1614 **Figure 7:** Scatterplots between Aeolus (y-axis) and ground-based (x-axis) backscatter coefficient retrievals resolved
 1615 based on the indices of Aeolus vertical bins (colored circles). In the upper (i) and bottom (ii) panels are depicted the
 1616 results for the unfiltered and filtered Aeolus profiles, respectively. On the left and right columns are illustrated the results
 1617 corresponding to Aeolus regular (24 bins) and mid-bin (23 bins) vertical scales, respectively. Aeolus backscatter values
 1618 larger than $20 \text{ Mm}^{-1} \text{ sr}^{-1}$ are masked out from the collocated sample.

1619